Chemical Geology 524 (2019) 11–36

Contents lists available at ScienceDirect

Chemical Geology

journal homepage: www.elsevier.com/locate/chemgeo

Cycles of trace elements and isotopes in the ocean - GEOTRACES and beyond

Dissolved rare earth elements distribution in the Solomon Sea

V.Q. Pham[a,e,*], M. Grenier[a], S. Cravatte[a], S. Michael[b], S. Jacquet[c], M. Belhadj[a], Y. Nachez[a], C. Germineaud[d], C. Jeandel[a]

[a] LEGOS, Université de Toulouse, (CNRS, UPS, IRD, CNES), Toulouse, France
[b] School of Oceanography, University of Washington, Seattle, WA 98105, USA
[c] Aix Marseille Université, CNRS/INSU, Université de Toulon, IRD, Mediterranean Institute of Oceanography (MIO), UM 110, 13288 Marseille, France
[d] Université Grenoble Alpes, CNRS, IRD, Grenoble-INP, IGE, Grenoble, France
[e] Department of Water- Environment- Oceanography, University of Science and Technology of Hanoi, 18 Hoang Quoc Viet, Cau Giay, Hanoi, Vietnam

ARTICLE INFO

Editor: Michael E. Böttcher

Keywords:
Solomon Sea
Coral Sea
Dissolved rare Earth Element distribution
Lithogenic inputs
GEOTRACES

ABSTRACT

Trace Elements and Isotopes (TEIs) were measured as part of the GEOTRACES PANDORA cruise (July–August 2012, R/V *L'Atalante*), among them Rare Earth Elements (REEs) as pertinent tracers of land-ocean inputs and water mass transformations. This work discusses results of 19 dissolved REE (dREE) profiles measured using a trispike method in the Coral Sea and inside and at the exits of the Solomon Sea, a semi-enclosed sea with complex topography and straits. Overall, dREEs –except the insoluble Ce– show nutrient like profiles, i.e. depleted at the surface and enriched at depth. Illustrative Nd concentrations range from ~5 pmol/kg at the surface to > 25 pmol/kg at 5000 m depth. However, local dREE enrichments are observed, mostly in the Straits (Indispensable, Solomon and Vitiaz Straits) and along the island coasts. A box model allows calculating and discussing the fate of the dREEs in the different water layers flowing through the Solomon Sea. Finally, subtle variations revealed by La, Ce, Eu anomalies and the normalized light versus heavy REE ratio (expressed as Nd_n/Yb_n) allows the identification of specific mechanisms affecting the distribution of the different dREEs. The positive Eu anomaly observed in the surface layers reflects the basaltic origin of external inputs, consistent with the intensive weathering and/or volcanic activity affecting the surrounding islands. These data also confirm that the distributions of heavy dREEs (like Yb) are better correlated to the dSi concentrations than that of the other REEs.

This article is part of a special issue entitled: "Cycles of trace elements and isotopes in the ocean – GEOTRACES and beyond" - edited by Tim M. Conway, Tristan Horner, Yves Plancherel, and Aridane G. González.

1. Introduction

In the southwest Pacific Ocean, the northern branch of the westward South Equatorial Current is conveyed equatorward by the low-latitude western boundary currents (LLWBCs, Fig. 1). These currents flow through the semi-enclosed Solomon Sea as a final pathway between the subtropical Pacific and the Equator (Fine et al., 1994; Grenier et al., 2014; Ganachaud et al., 2014). The LLWBCs join the equatorial current system, in particular the eastward Equatorial Undercurrent feeding the "cold equatorial tongue" in the eastern equatorial Pacific. The properties of the water masses they transport have thus the potential to impact the equatorial thermocline stratification as well as native ecosystems of the western Pacific with potential downstream effects on the eastern Pacific ones (Slemons et al., 2010; Qin et al., 2016). Hence, the Solomon Sea is a hot spot to study the water modifications when flowing from the Subtropical to the Equatorial region.

The Solomon Sea is surrounded by high and intensively weathered islands (Milliman et al., 1999). Together with its complex topography and hydrography, these characteristics make this area a potential source of trace elements to the waters flowing through it. Preceding studies aimed at characterizing the chemistry of the LLWBCs upstream and downstream of the Solomon Sea (i.e. Grenier et al., 2013, 2014; Slemons et al., 2010; Mackey et al., 2002; Zhang and Nozaki, 1996). However, the Solomon Sea itself has not been documented so far, becoming with time a sort of "missing piece" of the geochemical map of this area.

Two exploratory oceanographic cruises were undertaken in the framework of the SPICE (Southwest Pacific Ocean Circulation and Climate Experiment) and GEOTRACES (www.geotraces.org) programs (Ganachaud et al., 2014; Ganachaud et al., 2017). The Pandora cruise (July–August 2012) documented a large number of hydrographic and biogeochemical parameters in the Coral and Solomon Seas while the

* Corresponding author.
E-mail address: viet.pham@legos.obs-mip.fr (V.Q. Pham).

https://doi.org/10.1016/j.chemgeo.2019.05.012
Received 31 May 2018; Received in revised form 19 April 2019; Accepted 9 May 2019
Available online 28 May 2019
0009-2541/ © 2019 Elsevier B.V. All rights reserved.

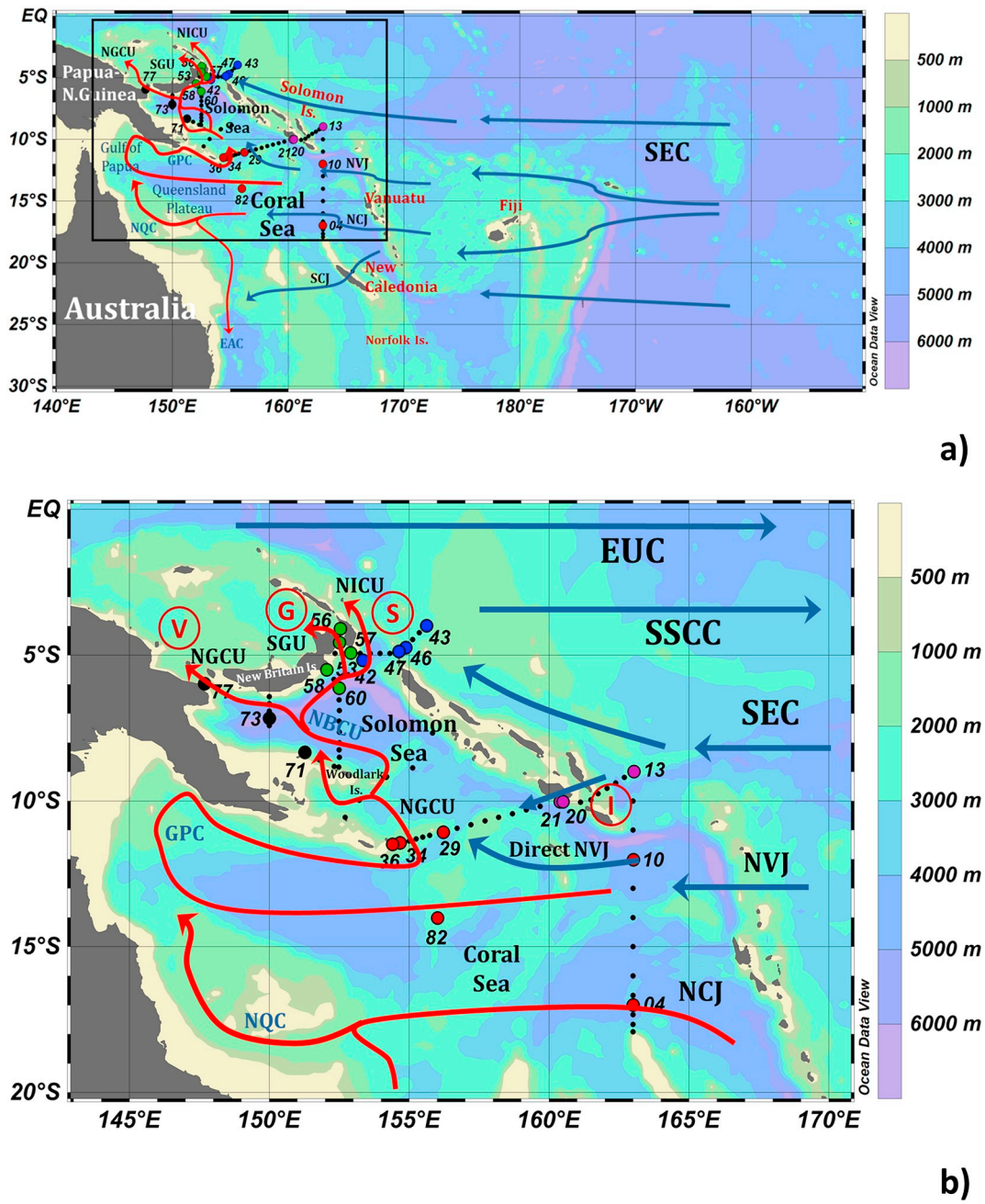

Fig. 1. General map of the studied area (a) and zoom panel in the Coral and Solomon Seas allowing the identification of the sampling locations. Red arrows indicate the LLWBCs (b). The sampling locations are represented by circles and different colors associated with distinct regions. The red circles correspond the Coral Sea and Southern entrance of the Solomon Sea. Samples collected in waters flowing through four straits (Indispensable, Vitiaz, St George's and Solomon), are colored with dark violet, black, green and dark blue, respectively. These color criteria will be kept throughout this work. The main currents flowing in the South Western Pacific Ocean are shown by solid arrow (Grenier et al., 2011, 2013). SEC: South Equatorial Current, NVJ: New Vanuatu Jet, NCJ: New Caledonia Jet, GPC: eastward Gulf of Papua Current, NQC: polarward New Queensland Current, NGCU: New Guinea Coastal Undercurrent, NBCU: New Britain Coastal Undercurrent, NICU: New Ireland Coastal Undercurrent, SSCC: South Subsurface Countercurrent, EUC: Equatorial Undercurrent. The main archipelago and islands are also reported in the map. Straits are identified by a character covered by red circle: Indispensable, Vitiaz, St. George and Solomon Strait also highlighted in the map as V, G and S, correspondingly.

MoorSPICE cruise repeated the hydrographic measurements in March 2014.

Dissolved chemical elements and their isotopes (geochemical tracers) provide key information that allow us to better understand and characterize water mass histories and sources of key nutrient species to the oceans (Crusius et al., 1996; Elrod et al., 2004; Haley et al., 2004; Johnson et al., 2003; Nozaki, 1986). Among the "tracer world", REEs and isotopic composition of neodymium are used to determine water mass pathways and quantify lithogenic enrichments and scavenging processes that potentially occur along these pathways (Goldstein and Hemming, 2003; Jeandel et al., 2013; Lacan and Jeandel, 2001; Tachikawa et al., 2003). REEs are a group of 14 elements displaying coherent characteristics from lanthanum (La) to lutetium (Lu). The light REEs (LREEs) refer to the lower atomic number REEs from 57 (La) to 61 (Nd); Samarium (Sm) Europium (Eu) and Gadolinium (Gd) stand for medium REEs (MREEs), while Dysprosium (Dy) to Lutetium are heavy REEs (HREEs). Within this group, the atomic weight increases while the atomic size decreases, yielding chemical fractionation to occur during geochemical processes. In the oceanic environment, most of the previous studies concluded that not only internal processes (i.e.: Akagi,

2013; Akagi et al., 2011; Byrne and Kim, 1990; De Baar et al., 1985a; Lee and Byrne, 1993; Schijf et al., 2015; Tachikawa et al., 1999) but also external ones including suspended sediments in estuaries, groundwater and porewater (i.e.: Nozaki and Alibo, 2003a; Nozaki and Alibo, 2003b; Sholkovitz et al., 1994; Rousseau et al., 2015; Wang and Yamada, 2007; Abbott et al., 2015) could fractionate the REEs. The internal processes can be resumed as dissolved-particulate exchanges over the water column that result from biological uptake-remineralization and/or adsorption-desorption onto reactive particle coatings and/or (co)precipitation-dissolution (Sholkovitz et al., 1994). In addition, dREEs could be released to the open ocean from river discharge, atmospheric dust, hydrothermal plume or exchange at the land-ocean interface, considered as external inputs (Elderfield, 1990; Elderfield and Sholkovitz, 1987; German and Elderfield, 1989; Johannesson et al., 2011; Haley et al., 2004; Sholkovitz and Szymczak, 2000). Clearly identifying these processes and their consequences on the oceanic REE distribution is therefore a key issue.

This work characterizes the dREE concentrations from surface to bottom at 21 stations collected between the entrance of the Coral Sea and the exiting straits of the Solomon Sea. The geochemical data are coupled with the associated hydrological parameters and the water mass transports to permit the discrimination and fine characterization of key processes occurring along the water mass pathways. This strategy allows us to describe and quantify the modification of geochemical parameters during equatorward transit of the waters through the Solomon Sea. Our results are also compared with other geochemical parameters (e.g. Al, Mn) which helps to validate the enrichment of lithogenic origin observed in the Solomon Sea. Relationships between dREEs and nutrient data are also discussed.

Section 2 describes the sampling procedure, sample preservation and analytical protocol while Section 3 presents the hydrological context. Section 4 presents the resulting dREE profiles and their PAAS-normalized patterns. Results are discussed in Section 5. A simple box model allows estimating the dREE Solomon Sea budgets in different density layers, and the water enrichment along their pathways. This section also presents a discussion around the fractionation observed in the REE patterns and the presumed associated mechanisms.

2. Material and methods

2.1. Sample collection

143 seawater samples were collected at 21 stations (19 dREE full profiles, one station with one deep sample and one total dissolved REE profile) during the PANDORA cruise (July–August 2012, onboard R/V *L'Atalante*). The sampling locations are reported in Fig. 1b. Nine stations (stations 04, 10, 13, 20, 21, 29, 34, 36 and 82) were located in the Coral Sea and at the southern entrance of the Solomon Sea. Stations 04 and 10 were sampled to characterize the North Vanuatu Jet (NVJ) and North Caledonia Jet (NCJ), respectively. Stations 13, 20 and 21 were collected before and after the Indispensable Strait in order to identify potential modifications of the water properties when flowing through this strait. Stations 29, 34 and 36 tried to catch the complex hydrological features at the entrance of the Solomon Sea (Cravatte et al., 2011; Davis et al., 2012; Germineaud et al., 2016). The remaining 12 stations are located in the "body" of the Solomon Sea as well as in the 3 straits through which waters flow out (i.e. Vitiaz Strait, St George's Channel and Solomon Strait).

Salinity (S), potential temperature (θ) and dissolved oxygen (dO_2) were measured on board using sensors mounted at the base of the rosette. Salinity and oxygen sensors were calibrated and adjusted after the cruise using the measurements of these parameters on discrete samples (Ganachaud et al., 2017). Shipboard and Lowered Acoustic Doppler Current Profiler (L-ADCP) data and other samples for various chemical analyses were also acquired during the cruise for the seawater characterization in trace metals, nutrients and other biological and chemical parameters. The online cruise report (http://www.obs-vlfr.fr/proof/php/pandora/xdatalist1.php?xxop=pandora&xxcamp=pandora) and the synthesis article of Ganachaud et al. (2017) provide more details on the numerous operations conducted in the framework of PANDORA.

Seawater samples dedicated to dREE analysis were collected using 12 L-Niskin bottles mounted on a standard rosette. Aliquots of 500 mL were rapidly filtered through 0.4 μM pore size, 47 mm diameter SUPOR membranes in the R/V *L'Atalante* humid laboratory. Filtered water was transferred into pre-cleaned low density polyethylene (LDPE) bottles and immediately acidified to pH ≤ 2 by addition of suprapur 30% HCl. All consumable material was acid-cleaned before the cruise. Note that samples from station 82 and some duplicates from station 73 and 77 were not filtered. Replicate samples were also taken at some stations in order to validate the data, identify particle-dissolved interaction and control the blank of the filtration system (e.g. at station 73).

2.2. Analytical procedure

dREE concentrations were determined using the LEGOS protocol (Lacan and Jeandel, 2001; Tachikawa et al., 1999). Briefly, dREEs were extracted from the seawater aliquot by a co-precipitation with iron hydroxides, followed by purification through ion-exchange column and measured with a High Resolution Inductively Coupled Plasma Mass Spectrometer (HR-ICP-MS). In details, a trispike solution containing ^{150}Nd (97.84%), ^{151}Eu (97.84%), and ^{172}Yb (94.9%) was added to the acidified seawater aliquots of 250 mL or 500 mL. Approximately 2.5 mg of purified $FeCl_3$ diluted in 0.1 M HCl was then added to the samples. The homogenization was ensured by a continuous shaking of the sample during 24 h and a subsequent 24 h resting state before performing the co-precipitation. Then, the pH was increased to 8 ± 0.5 by adding suprapur NH_4OH yielding the iron hydroxides to co-precipitate the dREEs. The dREE-Fe precipitate was then rinsed and separated from the seawater by successive centrifugations. This rinsing step was repeated up to 7 times and the precipitate was later dissolved in 1 mL of 6 M HCl and then loaded on an anion exchange column packed with 2 mL of AG1-X8 resin, in order to purify the dREE fraction from Fe. dREEs were then eluted from the column using 4 mL of 6 M HCl and evaporated to dryness. Finally, the residue was dissolved again with 5 mL 0.32 M HNO_3 spiked with an internal standard (In−Re, 100 ppt), which is the appropriate solution to measure the concentrations on a sector field Inductively Coupled Plasma Mass Spectrometer (THERMO ELEMENT XR™ ICP-MS).

Recoveries of the whole experiment (including sensitivity variations during the ICP-MS sequence) were precisely determined by comparing the Nd, Eu and Yb concentrations calculated by Isotopic Dilution (ID-CONC) with that measured by external calibration (EXT-CONC). The ratio (EXT-CONC)/(ID-CONC) for these 3 elements were then linearly interpolated and extrapolated to be applied to the remaining dREE concentrations, measured by external calibration only. On the average, recoveries of > 80% were obtained for the light REEs, and around 77% for the middle and heavy REEs. Our method, based on 2 or 3 spikes followed by interpolation (and extrapolation), was validated by comparing results obtained using 10 spikes on the same seawater samples, either in the framework of T. Rousseau thesis (Rousseau et al., 2013) or in the recent work of M. Behrens (Behrens et al., 2016). During the ICP-MS analysis, the use of a desolvating nebulizer system (ARIDUS II) considerably minimized the oxide interference formation (Chung et al., 2009; Grenier et al., 2013; Pahnke et al., 2012). This is notably effective for the barium oxide formation reduction, which subsequently improves the analytical accuracy for ^{151}Eu and ^{153}Eu.

Replicate measurements were conducted on filtered (4 replicates, station 73, 1650 m) and non-filtered samples (3 replicates at 1650 m of station 73 and 4 replicates at 1200 m of station 82). Filtered light REE (dLREE) concentrations agree within 8% for La, 14% for Ce and 4% for Pr and Nd; filtered middle (dMREE) and heavy (dHREE) concentrations agree within 8% for Sm, 11% for Eu and < 4% for the remaining REEs.

Non-filtered concentrations agree within < 4% for all the LREEs (including Ce) and 7% for MREEs and HREEs.

The average chemical blank values were established on 20 measurements. Blank levels represent < 2% of the LREE signals and < 0.7% for MREE and HREE ones. Due to the very low Ce concentrations in our samples, the dCe blanks represent 14 ± 9% of the sample signal. In addition, the blank of our on-board filtration system was checked by filtering twice the same samples. No noticeable variation of concentration was observed, assessing the cleanliness of our systems. Finally, our full dREE analytical procedure was validated by our successful participation to two GEOTRACES intercalibration exercises (Behrens et al., 2016; van de Flierdt et al., 2012).

Together with dREE analysis, the dissolved Ba were also measured following this protocol: 15 mL of unfiltered seawater were collected in pre-cleaned polypropylene bottles (rinsed three times with the same seawater sample), acidified with 15 μL of HCl (10 M, Optima grade) and kept at room temperature for later analysis. Dissolved Ba concentrations were measured using an isotope dilution (ID) method (Freydier et al., 1995; Klinkhammer and Chan, 1990) by high resolution -inductively coupled plasma- mass spectrometry (HR-ICP-MS), operated at low resolution mode. This method was adapted to a Thermo Finnigan Element XR™ instrument (MIO, Marseille). The dissolved Ba measurements presented here are the sum of dissolved Ba and a very small fraction (generally < 1% of total Ba) that is generated from the particulate Ba pool as a result of the acidification (Jacquet et al., 2005). For the sake of simplicity, we use the term of dissolved Ba and dBa data are reported in the Table B of Supplementary material. Samples (0.5 mL) were spiked with 300 μL of a ^{135}Ba-enriched solution (93% ^{135}Ba; 95 nmol/kg) and diluted with 15 mL of acidified (2% HNO3, 14 M, Optima grade) Milli-Q grade water (Millipore). The amounts of sample, spike and dilution water were assessed by weighing. Reproducibility of this method is 1.5% (1 RSD) as tested on repeated preparations of the reference solution SLRS-5 (NRC-CNRC river water reference material for trace metals; 101.9 ± 3.6 nmol/kg). The limit of detection, calculated as three times the standard deviation of the procedural blank, is 0.09 nmol/kg.

3. Hydrological context

Coral and Solomon Sea hydrological properties have been the subject of several surveys since the early 1960s. Water mass properties were discussed in miscellaneous works since then (e.g. Tsuchiya, 1981; Tsuchiya et al., 1989; Qu and Lindstrom, 2002; Grenier et al., 2013; Kessler and Cravatte, 2013; Ganachaud et al., 2014). Germineaud et al. (2016) presented a detailed description of the currents and water mass properties from the surface down to 1000 m depth based on both the PANDORA (2012) and MoorSPICE (2014) cruise data. The description proposed here is mostly based on this last work together with the thorough description given in Southwest Pacific currents conducted by Grenier et al. (2011, 2013, 2014). The water mass nomenclatures vary among authors; the names used in this study follow those proposed by Tomczak and Hao (1989) and adopted by Grenier et al. (2013) in order to avoid any confusion when describing the water masses, especially in the layers characterizing the thermocline.

The general circulation scheme, current names and sampling details of the different stations used in this study are given in Fig. 1. Fig. 2 proposes a compilation of hydrological property plots observed at the different stations, together with the identification of the main water masses sampled during the cruise. The last column of Table 1 recalls the water masses corresponding to the collected seawater samples.

Water properties in the Southwest Pacific can be traced from the Coral Sea to the Solomon Sea, in part through the Low Latitude Western Boundary Currents (LLWBCs) flowing toward the Equator (Fig. 1). The LLWBCs are initially fed by the westward South Equatorial Current (SEC; Qu and Lindstrom, 2002; Tsuchiya et al., 1989), dividing into several zonal currents when encountering islands in the Coral Sea. These zonal currents -some of them extending as deep as 1000 m- transport several water masses that we choose to describe here following increasing density.

3.1. Thermocline waters

3.1.1. Upper thermocline: tropical and equatorial waters

In the Coral and Solomon Seas, the upper thermocline is made of salty South Pacific Tropical Waters (SPTW) (~σ_θ = 24.3–25.3 kg/m^3). This tropical water can be divided into two main branches.

The northern branch of the SPTW is called the South Pacific Equatorial Water (SPEW) and enters the Coral Sea north of the Vanuatu Archipelago, transported by the North Vanuatu Jet (NVJ) (Kessler and Cravatte, 2013; Tomczak and Godfrey, 2003; Tomczak and Hao, 1989; Tsuchiya et al., 1989). The SPEW originates from the subtropical central South Pacific (~20°S, 110°W), characterized by high evaporation and a maximum in sea surface salinity (see Fig. 1 of Grenier et al., 2013). The SPEW is thus marked by a maximum in salinity (~S = 36.0) at ~σ_θ = 24.5 kg/m^3 (Kessler, 1999; Qu and Lindstrom, 2002) and relative high oxygen (~135 μmol/kg; Grenier et al., 2013). It enters the Solomon Sea both through a direct pathway in the middle of the southern entrance, and through the NGCU flowing along the coast. During Pandora, SPEW was well identified at station 10 (Fig. 2).

The southern branch of the SPTW enters the Coral Sea mainly south of the Vanuatu Archipelago, conveyed by the North Caledonian Jet (NCJ; Ganachaud et al., 2014; Gasparin et al., 2011; Germineaud et al., 2016; Grenier et al., 2013). At the entrance of the Coral Sea, this water mass is slightly denser (~σ_θ = 24.8 kg/m^3), less saline (S~35.6) and richer in oxygen (~165 μmol/kg^1) than those of the northern branch (see station 04, Fig. 2). It enters the Solomon Sea through the NGCU.

Inside the Solomon Sea, the NGCU splits south of Woodlark Island and then remerges at its northern side, to finally bifurcate again into two branches south of New Britain Island. The first branch flows westward toward the Bismarck Sea through Vitiaz Strait while the second one is conveyed eastward by the New Britain Coastal Undercurrent. It exits the Solomon Sea northward by the St George's Undercurrent (SGU) and the New Ireland Coastal Undercurrent (NICU) through St George's Channel and Solomon Strait, respectively (Cravatte et al., 2011; Ganachaud et al., 2014; Ganachaud et al., 2017; Germineaud et al., 2016). Since the SPTW in the Solomon Sea results from the mixing between two water masses of minor differences which are referred above, its characteristics are fairly high oxygen content (140–145 μmol/kg^1) and high salinity level (~S = 35.7, see stations 34, 36, 42, 43, 57, 60, 71, 73 and 77 in Fig. 2).

3.1.2. Lower thermocline: central water and mode water

Lying just underneath the upper thermocline water, the Western South Pacific Central Water (WSPCW), displays very loose stratification at about 300 m depth (Grenier et al., 2014; Qu et al., 2008; Tsuchiya, 1981). WSPCW is described by potential density centered at 26.4 kg/m^3 and high salinity due to its origin, north of New Zealand (Tomczak and Hao, 1989). Rich in oxygen (mean O_2 = 160 kg/m^3), the WSPCW is conveyed into the Coral Sea in its southern part, through the deep NCJ (Gasparin et al., 2011; Sokolov and Rintoul, 2000; Tomczak and Godfrey, 2003; Tsuchiya et al., 1989). While crossing the Solomon Sea, this water mass may become depleted in oxygen by mixing with water originating from the southeastern Pacific Ocean (Kessler and Cravatte, 2013).

Below the WSPCW flows a mode water. The Subantarctic Mode Water (SAMW; ~σ_θ = 26.5–27 kg/m^3; no salinity or oxygen extremum) enters the Coral and Solomon Seas from the south (Grenier et al., 2013; McCartney, 1977). It originates from the Southern Ocean by subduction north of the Antarctic Circumpolar Current (Hanawa and Talley, 2001). This water mass is centered on ~σ_θ = 27 kg/m^3 and is characterized by a low salinity (~34.5) and high oxygen content (~175 kg/m^3) because of its origin (Qu et al., 2009). In the Coral and Solomon Seas, the SAMW

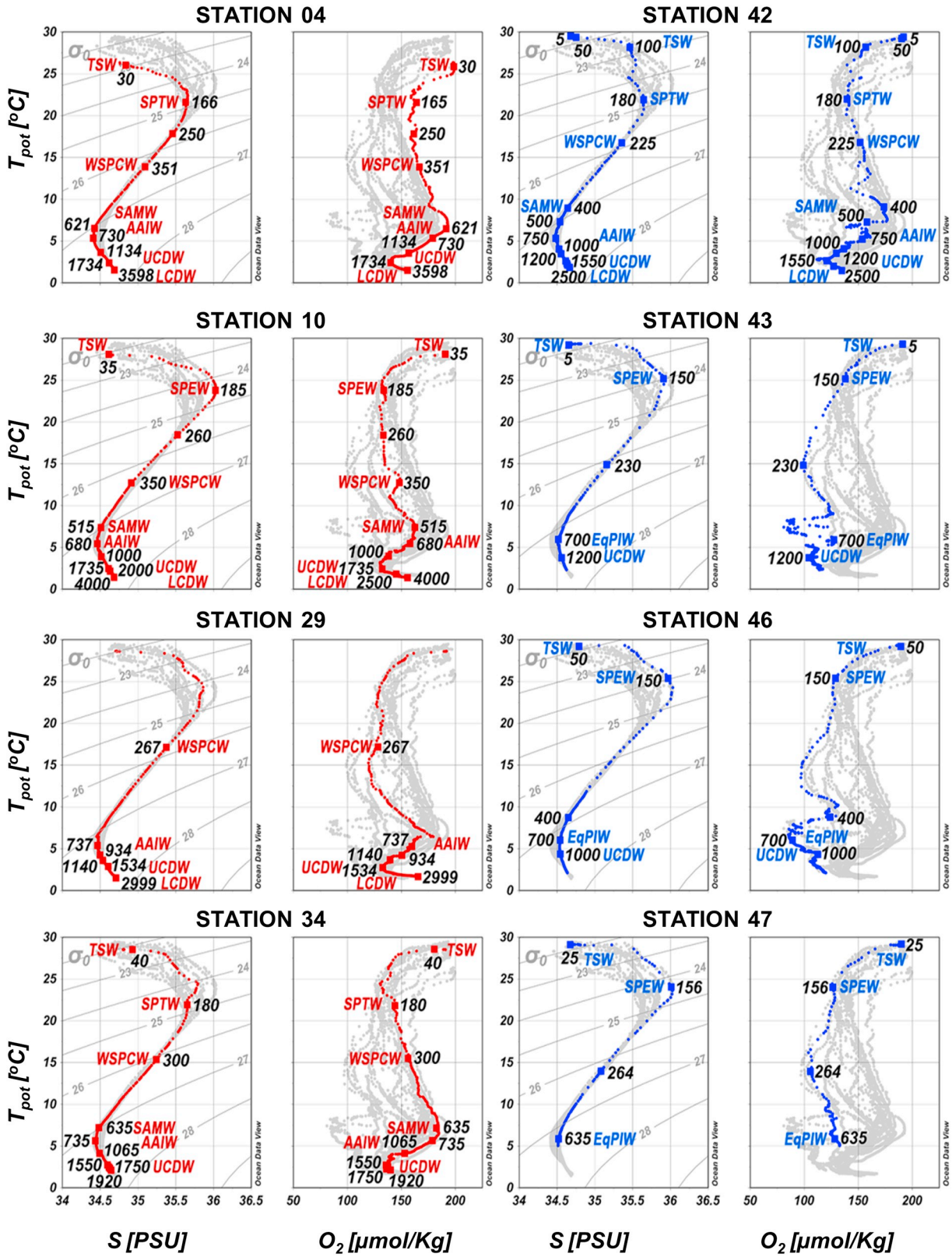

Fig. 2. Potential temperature (θ) versus salinity (S; right) and potential temperature (θ) versus dissolved oxygen (O_2; left) plots for the stations. The curve colors correspond to the different locations denoted in Fig. 1. The grey curves are representing the same properties at all the hydrographic stations sampled as part of PANDORA. In the left plots, potential density anomaly contours are shown as solid grey lines. Each depth sampled for dissolved REE measurement is identified by a rectangle and its value (m). All the data characterizing the stations represented here are provided in Table 1. The water masses at the sampling depth are also highlighted by their notation: TSW: Tropical Surface Water, SPTW: South Pacific Tropical Water, SPEW: South Pacific Equatorial Water, WSPCW: Western South Pacific Central Water, SAMW: Subantarctic Mode Water, AAIW: Antarctic Intermediate Water, EqPIW: Equatorial Pacific Intermediate Water, UCDW and LCDW: Upper and Lower Circumpolar Deep Water.

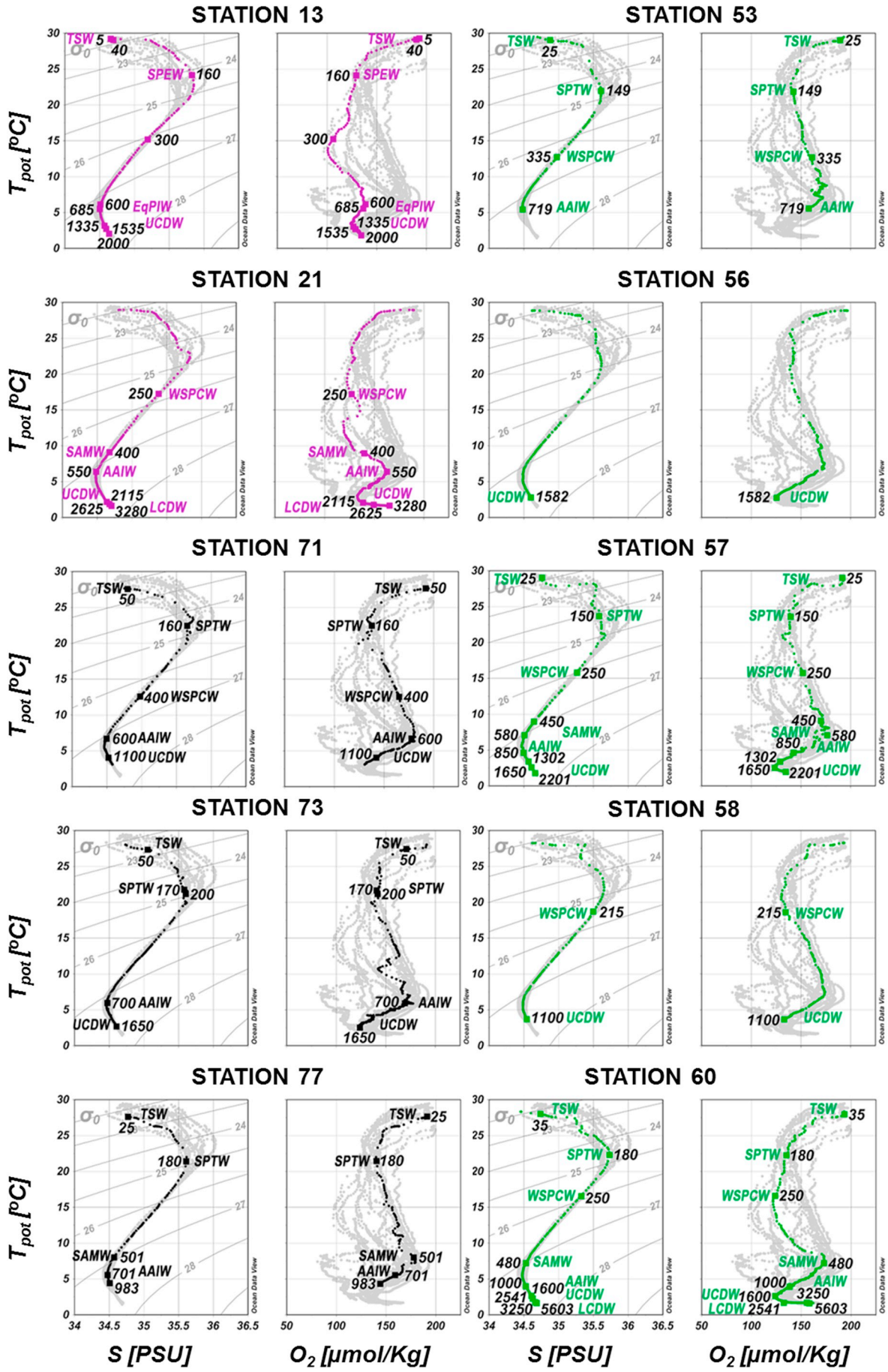

Fig. 2. (*continued*)

Table 1
Station number and locations, depths, hydrological properties, dREE anomalies of the analyzed samples; the corresponding water masses are identified.

Depth	Salinity	Pot. temp	O_2	Pot. dens	La/La*	Ce/Ce*	Eu/Eu*	Yb/Yb*	$(Nd/Yb)_n$	Water mass
(m)	(PSU)	[°C]	(μmol/kg)	(σ_0) (kg/m^3)						
Station 004 (July 01, 2012; 17° 0′ 10.8″ S; 162° 59′ 45.6″ E; depth: 4680 m)										
30	34.840	25.931	199	22.94	2.08	0.60	1.21	0.50	0.25	TSW
166	35.631	21.533	164	24.83	1.81	0.51	1.12	0.50	0.22	SPTW
250	35.462	17.831	161	25.67	2.31	0.46	1.11	0.55	0.21	
351	35.095	13.923	167	26.28	2.04	0.23	1.09	0.59	0.17	WSPCW
621	34.426	6.496	192	27.04	2.11	0.12	1.00	0.66	0.14	SAMW
730	34.415	5.375	179	27.17	2.21	0.10	1.11	0.70	0.13	AAIW
1134	34.510	3.573	157	27.44	2.20	0.41	1.05	0.74	0.13	
1734	34.620	2.410	140	27.64	–	–	–	–	–	UCDW
3598	34.687	1.546	156	27.76	5.48	0.09	1.12	0.77	0.22	LCDW
Station 010 (July 03, 2012; 12° 0′ 0″ S; 162° 59′ 56.4″ E; depth: 5092 m)										
35	34.616	28.053	191	22.09	2.13	0.51	1.21	0.50	0.26	TSW
185	36.029	24.496	134	24.50	–	–	–	–	–	SPEW
260	35.523	18.403	133	25.58	2.12	0.29	1.21	0.54	0.20	
350	34.918	12.675	148	26.40	2.68	0.27	1.05	0.60	0.18	WSPCW
515	34.510	7.400	163	26.98	–	–	–	–	–	SAMW
680	34.458	5.395	158	27.20	2.61	0.10	0.95	0.72	0.12	AAIW
1000	34.520	3.960	139	27.41	–	–	–	–	–	
1735	34.613	2.435	133	27.63	2.62	0.14	1.12	0.77	0.13	UCDW
2500	34.669	1.777	145	27.73	2.26	0.07	1.13	0.75	0.17	LCDW
4000	34.685	1.443	153	27.77	2.14	0.13	1.08	0.77	0.20	
Station 013 (July 04, 2012; 9° 0′ 10.8″ S; 162° 59′ 56.4″ E; depth: 3853 m)										
5	34.651	29.182	191	21.74	1.74	0.61	1.14	0.45	0.34	TSW
40	34.675	29.157	191	21.77	1.77	0.54	1.05	0.44	0.29	
160	35.830	24.121	129	24.24	3.32	0.74	1.26	0.53	0.19	SPEW
300	35.188	15.244	106	26.07	2.54	0.26	0.96	0.57	0.18	–
600	34.515	6.128	138	27.16	3.52	0.10	1.08	0.72	0.12	EqPIW
685	34.503	5.528	138	27.22	2.89	0.14	1.18	0.71	0.12	
1335	34.574	3.108	126	27.54	4.01	0.15	1.02	0.75	0.11	UCDW
1535	34.595	2.709	129	27.60	4.86	0.10	1.11	0.78	0.12	
2000	34.640	2.023	133	27.69	3.19	0.11	1.21	0.80	0.14	
Station 020 (July 06, 2012; 9° 59′ 56.4″ S; 160° 25′ 1.2″ E; depth: 2910 m)										
25	34.832	28.896	189	21.97	2.09	0.56	1.21	0.56	0.27	TSW
190	35.822	22.620	127	24.67	–	–	–	–	–	SPEW
600	34.485	6.223	162	27.12	3.49	0.19	1.02	0.71	0.13	AAIW
900	34.490	4.787	151	27.30	3.53	0.12	1.08	0.72	0.12	
1600	34.599	2.720	133	27.60	–	–	–	–	–	UCDW
Station 021 (July 07, 2012; 10° 0′ 46.8″ S; 160° 21′ 25.2″ E; depth: 3342 m)										
250	35.388	17.226	127	25.76	3.05	0.35	1.08	0.53	0.20	WSPCW
400	34.675	9.036	140	26.86	3.24	0.19	1.07	0.69	0.13	SAMW
550	34.491	6.382	163	27.10	3.06	0.11	1.06	0.71	0.12	AAIW
2115	34.644	2.075	139	27.69	3.48	0.10	1.20	0.80	0.16	UCDW
2625	34.677	1.787	150	27.74	3.52	0.09	1.14	0.79	0.15	LCDW
3280	34.700	1.614	165	27.77	3.07	0.09	1.14	0.76	0.18	
Station 029 (July 09, 2012; 11° 3′ 39.6″ S; 156° 12′ 54″ E; depth: 3856 m)										
267	35.378	17.122	128	25.78	2.49	0.35	1.10	0.53	0.20	–
737	34.465	5.346	160	27.21	3.32	0.18	1.07	0.73	0.12	AAIW
934	34.497	4.281	150	27.36	3.29	0.28	1.08	0.74	0.13	
1140	34.535	3.704	139	27.45	3.37	0.16	1.16	0.74	0.12	
1534	34.593	2.817	133	27.59	3.65	0.08	1.16	0.76	0.13	UCDW
2999	34.699	1.687	166	27.77	3.02	0.10	1.14	0.77	0.17	LCDW
Station 034 (July 10, 2012; 11° 27′ 7.2″ S; 154° 39′ 54″ E; depth: 2005 m)										
40	34.932	28.522	181	22.17	2.47	0.54	1.21	0.55	0.23	TSW
180	35.656	21.834	144	24.77	3.76	0.50	1.21	0.57	0.20	SPTW
300	35.247	15.416	156	26.08	2.46	0.30	1.14	0.60	0.18	WSPCW
635	34.485	7.121	183	27.00	2.19	0.23	1.01	0.67	0.14	SAMW
735	34.439	5.649	179	27.16	1.94	0.39	1.04	0.69	0.15	AAIW
1065	34.493	4.140	154	27.37	3.23	0.24	1.05	0.71	0.13	
1550	34.600	2.730	136	27.60	3.02	0.15	1.05	0.73	0.14	UCDW
1665	34.613	2.558	137	27.62	3.42	0.09	1.11	0.74	0.14	
1750	34.625	2.385	136	27.65	2.88	0.10	1.11	0.74	0.15	
1920	34.645	2.140	140	27.69	–	–	–	–	–	
Station 036 (July 11, 2012; 11° 30′ 7.2″ S; 154° 23′ 24″ E; depth: 1168 m)										
24	34.489	27.756	195	22.09	1.52	0.54	1.25	0.59	0.34	TSW
101	35.431	24.271	163	23.89	2.31	0.56	1.18	0.55	0.22	
159	35.609	22.290	141	24.60	2.28	0.50	1.22	0.54	0.22	SPTW
180	35.639	21.074	144	24.96	2.60	0.56	1.11	0.55	0.22	
401	34.943	12.203	167	26.51	2.37	0.23	1.08	0.63	0.16	WSPCW
699	34.460	6.285	182	27.09	2.75	0.12	0.98	0.69	0.13	AAIW

(*continued on next page*)

Table 1 (*continued*)

Depth (m)	Salinity (PSU)	Pot. temp [°C]	O_2 (μmol/kg)	Pot. dens (σ_θ) (kg/m^3)	La/La*	Ce/Ce*	Eu/Eu*	Yb/Yb*	$(Nd/Yb)_n$	Water mass
901	34.458	5.126	170	27.24	3.03	0.12	1.07	0.71	0.12	
Station 042 (July 15, 2012; 5° 8′ 42″ S; 153° 17′ 24″ E; depth: 3081 m)										
5	34.691	29.381	192	21.71	2.50	0.61	1.26	0.50	0.29	TSW
50	34.753	29.380	192	21.75	–	–	–	–	–	
100	35.464	28.210	157	22.68	–	–	–	–	–	
180	35.648	21.971	140	24.72	2.62	0.50	1.21	0.55	0.20	SPTW
225	35.353	16.762	152	25.85	2.99	0.26	0.79	0.57	0.17	WSPCW
400	34.644	9.024	174	26.84	2.99	0.19	0.98	0.67	0.14	SAMW
500	34.538	7.266	158	27.02	2.79	0.16	1.03	0.70	0.13	
750	34.484	5.316	154	27.23	3.24	0.15	1.06	0.73	0.12	AAIW
1000	34.526	4.032	137	27.41	3.01	0.14	1.07	0.73	0.13	
1200	34.557	3.501	130	27.49	3.31	0.18	1.22	0.77	0.13	
1550	34.610	2.607	123	27.62	3.15	0.22	1.22	0.78	0.15	UCDW
1750	34.621	2.419	124	27.64	3.99	0.20	1.16	0.78	0.15	
2000	34.639	2.132	126	27.68	3.03	0.13	1.22	0.76	0.16	
2500	34.660	1.782	133	27.73	3.02	0.15	1.20	0.78	0.18	LCDW
Station 043 (July 17, 2012; 3° 59′ 52.8″ S; 155° 35′ 38.4″ E; depth: 1925 m)										
5	34.659	29.274	191	21.72	2.34	0.57	1.13	0.44	0.29	TSW
150	35.914	25.138	138	23.99	2.65	0.49	1.12	0.55	0.20	SPEW
230	35.161	14.819	99	26.14	[6.85]	[1.32]	[1.19]	[0.64]	[0.17]	–
700	34.513	5.914	128	27.18	3.35	0.16	1.24	0.72	0.13	EqPIW
1200	34.564	3.737	105	27.47	3.31	0.13	1.15	0.79	0.12	UCDW
Station 046 (July 18, 2012; 4° 42′ 0″ S; 154° 52′ 48″ E; depth: 3117 m)										
50	34.794	29.190	190	21.85	2.67	0.49	1.19	0.42	0.30	TSW
150	35.974	25.365	129	23.97	3.29	0.36	1.11	0.52	0.18	SPEW
400	34.649	8.724	124	26.89	3.52	0.26	1.11	0.68	0.14	–
700	34.542	6.028	89	27.19	3.34	0.09	1.10	0.72	0.12	EqPIW
1000	34.540	4.326	112	27.39	3.43	0.15	1.07	0.75	0.13	UCDW
Station 047 (July 18, 2012; 4° 56′ 2.4″ S; 154° 38′ 52.8″ E; depth: 1004 m)										
25	34.670	29.108	190	21.78	1.99	0.50	1.27	0.51	0.30	TSW
156	36.017	24.025	126	24.41	3.80	0.63	0.99	0.51	0.18	SPEW
264	35.082	13.952	106	26.27	2.71	0.22	1.05	0.63	0.16	–
635	34.522	5.856	129	27.20	2.92	0.21	1.09	0.72	0.13	EqPIW
Station 053 (July 19, 2012; 4° 54′ 18″ S; 152° 52′ 12″ E; depth: 733 m)										
25	34.879	28.959	189	21.99	2.55	0.57	1.27	0.57	0.26	TSW
149	35.610	21.864	142	24.72	3.30	0.89	1.12	0.55	0.23	SPTW
335	34.977	12.632	161	26.45	2.57	0.21	1.10	0.65	0.16	WSPCW
719	34.480	5.424	158	27.22	3.17	0.12	1.07	0.71	0.13	AAIW
Station 056 (July 20, 2012; 4° 4′ 37.2″ S; 152° 32′ 20.4″ E; depth: 1580 m)										
1582	34.599	2.818	125	27.59	3.20	0.18	1.08	0.72	0.15	UCDW
Station 057 (July 20, 2012; 4° 34′ 12″ S; 152° 31′ 22.8″ E; depth: 2552 m)										
25	34.767	28.952	192	21.91	3.16	0.59	1.39	0.55	0.27	TSW
150	35.583	23.624	139	24.20	2.52	0.52	1.19	0.55	0.21	SPTW
250	35.268	15.802	152	26.00	2.45	0.32	1.09	0.58	0.18	WSPCW
450	34.650	8.974	171	26.85	2.94	0.16	1.02	0.71	0.14	
580	34.509	7.083	177	27.02	2.85	0.22	1.06	0.69	0.13	SAMW
850	34.503	4.623	143	27.33	3.53	0.14	1.15	0.76	0.12	AAIW
1302	34.565	3.374	129	27.51	4.17	0.18	1.18	0.77	0.13	UCDW
1650	34.611	2.610	124	27.62	–	–	–	–	–	
2201	34.654	1.992	135	27.71	3.77	0.13	1.20	0.79	0.17	LCDW
Station 058 (July 21, 2012; 5° 30′ 10.8″ S; 152° 5′ 52.8″ E; depth: 1142 m)										
215	35.500	18.602	135	25.51	2.74	0.40	1.16	0.56	0.20	WSPCW
1100	34.547	3.675	133	27.47	3.77	0.20	1.07	0.76	0.13	UCDW
Station 060 (July 22, 2012; 6° 10′ 1.2″ S; 152° 29′ 49.2″ E; depth: 5609 m)										
35	34.737	28.022	193	22.19	2.03	0.59	1.30	0.54	0.30	TSW
180	35.733	22.267	135	24.70	2.40	0.44	1.18	0.52	0.22	SPTW
250	35.325	16.605	124	25.86	3.65	0.55	1.22	0.58	0.19	WSPCW
480	34.531	7.193	173	27.03	2.97	0.25	1.08	0.72	0.13	SAMW
1000	34.530	3.930	138	27.43	3.68	0.19	1.20	0.74	0.13	AAIW
1600	34.611	2.604	124	27.62	3.08	0.22	1.18	0.79	0.15	UCDW
1800	34.631	2.263	125	27.67	3.11	0.29	1.16	0.77	0.17	
2541	34.661	1.724	132	27.73	3.21	0.10	1.28	0.81	0.19	LCDW
3250	34.692	1.673	155	27.76	2.81	0.14	1.31	0.83	0.22	
4000	34.696	1.665	158	27.77	2.62	0.13	1.28	0.81	0.23	
4500	34.696	1.660	160	27.77	2.31	0.16	1.34	0.79	0.23	
4750	34.697	1.656	160	27.77	2.26	0.27	1.29	0.75	0.25	
5000	34.697	1.653	161	27.77	3.43	0.15	1.29	0.72	0.22	
5603	34.697	1.649	162	27.77	2.30	0.12	1.19	0.75	0.24	

(*continued on next page*)

Table 1 (*continued*)

Depth	Salinity	Pot. temp	O_2	Pot. dens	La/La*	Ce/Ce*	Eu/Eu*	Yb/Yb*	$(Nd/Yb)_n$	Water mass
(m)	(PSU)	[°C]	(μmol/kg)	(σ_θ) (kg/m^3)						
Station 071 (July 25, 2012; 8° 19′ 55.2″ S; 151° 17′ 27.6″ E; depth: 1563 m)										
50	34.797	27.552	192	22.39	2.14	0.46	1.26	0.52	0.24	TSW
160	35.659	22.424	138	24.60	5.68	1.37	1.09	0.52	0.22	SPTW
400	34.977	12.552	165	26.47	4.17	0.67	1.08	0.63	0.17	WSPCW
600	34.493	6.699	178	27.06	3.00	0.17	1.00	0.71	0.13	AAIW
1100	34.522	4.051	143	27.41	5.89	0.36	1.17	0.74	0.13	UCDW
Station 073 (July 26, 2012; 7° 9′ 57.6″ S; 149° 59′ 56.4″ E; depth: 5253 m)										
50	35.058	27.325	171	22.66	2.40	0.55	1.22	0.55	0.24	TSW
170	35.586	21.658	141	24.76	2.40	0.44	1.33	0.55	0.21	SPTW
200	35.602	21.191	140	24.90	2.85	0.36	1.15	0.53	0.19	
700	34.474	5.882	169	27.16	3.24	0.11	1.12	0.71	0.12	AAIW
1650	34.609	2.604	123	27.62	3.35	0.13	1.18	0.77	0.14	UCDW
Station 077 (July 28, 2012; 5° 57′ 3.6″ S; 147° 39′ 36″ E; depth: 1045 m)										
25	34.767	27.606	191	22.35	4.19	0.53	1.24	0.57	0.26	TSW
180	35.609	21.401	140	24.85	2.52	0.48	1.12	0.53	0.21	SPTW
501	34.572	8.016	178	26.94	2.43	0.37	1.09	0.71	0.16	SAMW
701	34.477	5.536	159	27.20	3.00	0.13	1.05	0.71	0.13	AAIW
983	34.505	4.473	145	27.35	3.73	0.19	1.13	0.74	0.13	
Station 082- non-filtrated (August 03, 2012; 13° 59′ 49.2″ S; 156° 0′ 25.2″ E; depth: 2586 m)										
25	34.927	26.195	197	22.92	2.68	0.72	1.40	0.53	0.26	TSW
180	35.789	22.612	129	24.65	3.06	0.82	1.04	0.53	0.21	SPTW
700	34.469	6.035	165	27.13	2.55	0.32	1.00	0.67	0.14	AAIW
800	34.451	5.083	163	27.23	2.65	0.29	1.02	0.68	0.13	
1000	34.498	4.114	151	27.38	3.14	0.92	1.04	0.71	0.13	
1200	34.539	3.454	145	27.48	3.60	0.44	1.05	0.74	0.12	UCDW
1350	34.565	3.159	140	27.53	3.45	0.17	0.98	0.73	0.13	
2000	34.636	2.226	141	27.67	2.29	0.37	1.18	0.77	0.14	

keeps its original characteristics and contributes to the formation of 13 °C Water (Qu et al., 2009).

3.2. Intermediate waters

The Antarctic Intermediate Water (AAIW; σ_θ~27.2 kg/m^3) is identified in the southern part of the studied region by a salinity minimum (~S = 34.3–34.5) and an oxygen maximum (~O_2 = 200–300 μmol/kg, Qu and Lindstrom, 2004). It enters the Solomon Sea via the NGCU (Bostock et al., 2010; Germineaud et al., 2016; Qu and Lindstrom, 2004; Tomczak and Godfrey, 2003). From the Coral Sea to the equator, the AAIW becomes slightly denser and less oxygenated (~σ_θ = 27.26 kg/m^3; O_2 = 160–190 μmol/kg) due to remineralization of organic material settling from the surface and to diapycnal mixing with lower oxygenated waters.

The Equatorial Pacific Intermediate Water (EqPIW; ~σ_θ = 27.3 kg/m^3), originally formed from a combination of AAIW and upwelled Pacific Deep Water (Bostock et al., 2010), is also identified. It is suggested that part of this water mass enters the Solomon Sea from the north-east through Solomon Strait (Germineaud et al., 2016) and mixes then with AAIW as proposed in Fig. 1 of Bostock et al. (2010). The distinct characteristics of this water mass is a salinity higher than that of AAIW (~S = 34.5–34.6) and a significantly lower oxygen concentration (~O_2 = 75–125 μmol/kg). It is found at a density of 27 kg/m^3 at station 43 and 46. Moreover, the oxygen plot of station 43 shows that EqPIW and AAIW form interleaving near 700 m depth (see Fig. 2).

3.3. Deep and bottom waters

The deep and bottom waters within the Coral and Solomon Seas have been poorly documented since the first observations summarized in Reid (1986, 1997) and their pathways and fates are not clearly understood. They are strongly constrained by the topography (Johnson and Toolet, 1993; Kawabe and Fujio, 2010; Roemmich et al., 1996; Tsimplis et al., 1998). Their pathways, origins and properties are the topic of an ongoing work.

The Upper Circumpolar Deep Water (UCDW) is observed between 1000 m and around 3500 m in the studied area. This water mass has been depleted in oxygen since its origin in the Antarctic Circumpolar Current (ACC; Reid, 1986; Talley, 2007; Wijffels et al., 2001). In this study, the UCDW is characterized by a relatively high salinity and a low oxygen content with a pronounced minimum (~S = 34.6, ~O_2 = 140 μmol/kg) at ~σ_θ = 27.65 kg/m^3 at almost all of our stations (Fig. 2). Germineaud et al. (2016) suggests that the UCDW can be divided into two sublayers, the upper extent (σ_θ~27.4–27.65 kg/m^3) and lower extent UCDW (σ_θ~27.65–27.76 kg/m^3).

Just beneath the UCDW, the Lower Circumpolar Deep Water (LCDW; Kawabe and Fujio, 2010; Reid, 1997; Tsimplis et al., 1998) is identified by a salinity maximum reaching 34.72–34.73 and a decrease of its silicate content when compared to the UCDW (Orsi et al., 1999).

4. Results

4.1. Dissolved REE concentrations

The dissolved concentrations measured for the 14 REEs at the different stations are compiled in Table 2. For simplicity, only the vertical distributions of dissolved lanthanum (dLa), neodymium (dNd), europium (dEu) and ytterbium (dYb) are shown in Fig. 3. dLa and dNd represent the dissolved LREEs while dEu and dYb represent the dMREEs and dHREEs, respectively.

The dREE concentrations display low values at the surface and increase with depth, showing a vertical profile shape similar to that of nutrients although not completely depleted in the surface waters (Fig. 3). dLa concentrations increase from ~4 pmol/kg in the surface water to ~15 pmol/kg at ~1000 m; dNd profiles vary from ~5 pmol/kg in the surface to ~10 pmol/kg at intermediate layer followed by a ~2.5-fold increase toward the bottom. Typical dEu and dYb profiles show the same kind of gradients as dLa and dNd, although with lower concentrations (< 1 pmol/kg for dEu and < 10 pmol/kg for dYb).

Table 2
Dissolved REE concentrations (pmol/kg). Data are reported with daily confidence interval (2σ).

Depth	Salinity	O_2	σ_θ	La	Ce	Pr	Nd	Sm	Eu	Gd	Tb	Dy	Ho	Er	Tm	Yb	Lu
(m)	(PSU)	(μmol/kg)	(kg/m^3)	(pmol/kg)													
Station 004 (July 01, 2012; 17° 0′ 10.8″ S; 162° 59′ 45.6″ E; depth: 4680 m)																	
30	34.84	199	22.94	3.7 ± 0.1	3.3 ± 0.1	0.8 ± 0	3.8 ± 0.1	0.9 ± 0	0.3 ± 0	1.5 ± 0.1	0.2 ± 0	1.8 ± 0.1	0.5 ± 0	1.6 ± 0.1	0.2 ± 0	1 ± 0	0.2 ± 0
166	35.63	164	24.83	3.3 ± 0.1	2.6 ± 0.1	0.7 ± 0	3.2 ± 0.1	0.8 ± 0	0.2 ± 0	1.2 ± 0.1	0.2 ± 0	1.5 ± 0.1	0.4 ± 0	1.5 ± 0.1	0.2 ± 0	1 ± 0	0.2 ± 0
250	35.46	161	25.67	4.1 ± 0.2	2.4 ± 0.1	0.7 ± 0	3.4 ± 0.1	0.8 ± 0	0.2 ± 0	1.2 ± 0	0.2 ± 0	1.6 ± 0.1	0.4 ± 0	1.5 ± 0.1	0.2 ± 0	1.1 ± 0	0.2 ± 0
351	35.10	167	26.28	6.2 ± 0.2	1.8 ± 0	1 ± 0	4.5 ± 0.1	0.9 ± 0	0.3 ± 0	1.6 ± 0.1	0.2 ± 0	2 ± 0.1	0.6 ± 0	2.2 ± 0.1	0.3 ± 0	1.8 ± 0	0.3 ± 0
621	34.43	192	27.04	11.8 ± 0.5	1.6 ± 0.1	1.7 ± 0.1	7.3 ± 0.2	1.7 ± 0.1	0.4 ± 0	2.5 ± 0.1	0.4 ± 0	3.4 ± 0.1	1 ± 0	3.9 ± 0.3	0.6 ± 0	3.7 ± 0.1	0.7 ± 0
730	34.42	179	27.17	12.3 ± 0.6	1.3 ± 0.1	1.8 ± 0.1	7.7 ± 0.4	1.5 ± 0.1	0.5 ± 0	2.8 ± 0.1	0.4 ± 0	3.6 ± 0.2	1.1 ± 0.1	4.2 ± 0.2	0.7 ± 0	4.1 ± 0.1	0.8 ± 0
1134	34.51	157	27.44	19 ± 0.7	8.3 ± 0.3	2.5 ± 0.1	10.3 ± 0.3	2 ± 0.1	0.6 ± 0	3.5 ± 0.2	0.5 ± 0	4.7 ± 0.3	1.4 ± 0.1	5.4 ± 0.3	0.9 ± 0	5.7 ± 0.2	1.1 ± 0
1734	34.62	140	27.64	–	–	–	–	–	–	–	–	–	–	–	–	–	–
3598	34.69	156	27.76	33.5 ± 1.3	2.4 ± 0.1	4.8 ± 0.2	24.1 ± 0.7	3.8 ± 0.2	1.1 ± 0	6 ± 0.3	0.9 ± 0	7.4 ± 0.3	2.1 ± 0.1	7.4 ± 0.4	1.2 ± 0.1	7.7 ± 0.3	1.4 ± 0.1
Station 010 (July 03, 2012; 12° 0′ 0″ S; 162° 59′ 56.4″ E; depth: 5092 m)																	
35	34.62	191	22.09	3.4 ± 0.1	2.6 ± 0.1	0.8 ± 0	3.6 ± 0.1	0.8 ± 0	0.3 ± 0	1.5 ± 0.1	0.2 ± 0	1.7 ± 0.1	0.5 ± 0	1.5 ± 0.1	0.2 ± 0	1 ± 0	0.2 ± 0
185	36.03	134	24.50	–	–	–	–	–	–	–	–	–	–	–	–	–	–
260	35.52	133	25.58	5.2 ± 0.2	1.8 ± 0.1	0.8 ± 0	3.6 ± 0.1	0.7 ± 0	0.2 ± 0	1.2 ± 0.1	0.2 ± 0	1.6 ± 0.1	0.5 ± 0	1.6 ± 0.1	0.2 ± 0	1.2 ± 0	0.2 ± 0
350	34.92	148	26.40	7.4 ± 0.3	2.1 ± 0.1	1.1 ± 0	4.9 ± 0.2	0.9 ± 0	0.3 ± 0	1.7 ± 0.1	0.3 ± 0	2.2 ± 0.1	0.6 ± 0	2.3 ± 0.1	0.3 ± 0	1.9 ± 0.1	0.3 ± 0
515	34.51	163	26.98	–	–	–	–	–	–	–	–	–	–	–	–	–	–
680	34.46	158	27.20	13 ± 0.5	[1.3 ± 0.1]	1.7 ± 0.1	7.7 ± 0.2	1.5 ± 0.1	0.4 ± 0	2.6 ± 0.1	0.4 ± 0	3.7 ± 0.2	1.1 ± 0.1	4.2 ± 0.2	0.7 ± 0	4.3 ± 0.1	0.8 ± 0.1
1000	34.52	139	27.41	–	–	–	–	–	–	–	–	–	–	–	–	–	–
1735	34.61	133	27.63	24.4 ± 1	3.2 ± 0.1	3 ± 0.1	13.1 ± 0.3	2.4 ± 0.1	0.8 ± 0	4.3 ± 0.2	0.7 ± 0	5.7 ± 0.3	1.7 ± 0.1	6.3 ± 0.3	1 ± 0	6.8 ± 0.2	1.3 ± 0.1
2500	34.67	145	27.73	31 ± 1.5	2.2 ± 0.1	4.3 ± 0.2	18.5 ± 0.6	3.5 ± 0.2	1.1 ± 0.1	5.6 ± 0.3	0.9 ± 0	7.1 ± 0.4	2.1 ± 0.1	7.3 ± 0.4	1.1 ± 0.1	7.6 ± 0.3	1.4 ± 0.1
4000	34.69	153	27.77	39.1 ± 1.3	5.9 ± 0.2	5.8 ± 0.2	24.6 ± 0.7	4.7 ± 0.2	1.3 ± 0.1	7.2 ± 0.3	1.1 ± 0	8.5 ± 0.4	2.4 ± 0.1	8.3 ± 0.4	1.3 ± 0	8.6 ± 0.3	1.6 ± 0.1
Station 013 (July 04, 2012; 9° 0′ 10.8″ S; 162° 59′ 56.4″ E; depth: 3853 m)																	
5	34.65	191	21.74	4 ± 0.1	3.8 ± 0.1	0.9 ± 0	3.9 ± 0.1	0.8 ± 0.1	0.2 ± 0	1.3 ± 0.1	0.2 ± 0	1.6 ± 0.1	0.4 ± 0	1.4 ± 0	0.2 ± 0	0.8 ± 0	0.1 ± 0
40	34.68	191	21.77	3.3 ± 0.1	2.8 ± 0.1	0.7 ± 0	3.3 ± 0	0.7 ± 0	0.2 ± 0	1.2 ± 0	0.2 ± 0	1.5 ± 0	0.4 ± 0	1.4 ± 0	0.2 ± 0	0.8 ± 0	0.1 ± 0
160	35.83	129	24.24	4 ± 0.1	2.9 ± 0.1	0.6 ± 0	2.8 ± 0.1	0.6 ± 0	0.2 ± 0	1.1 ± 0	0.2 ± 0	1.4 ± 0.1	0.4 ± 0	1.4 ± 0	0.2 ± 0	1 ± 0	0.2 ± 0
300	35.19	106	26.07	5.6 ± 0.1	[1.6 ± 0]	0.8 ± 0	3.7 ± 0.1	0.7 ± 0	0.2 ± 0	1.3 ± 0	0.2 ± 0	1.7 ± 0.1	0.5 ± 0	1.9 ± 0.1	0.3 ± 0	1.5 ± 0	0.3 ± 0
600	34.52	138	27.16	11.8 ± 0.2	[1 ± 0]	1.5 ± 0	7.2 ± 0.1	1.4 ± 0	0.5 ± 0	2.5 ± 0.1	0.4 ± 0	3.5 ± 0.1	1.1 ± 0	4 ± 0.1	0.6 ± 0	4.1 ± 0.1	0.8 ± 0
685	34.50	138	27.22	12.2 ± 0.5	1.6 ± 0.1	1.6 ± 0	7.2 ± 0.2	1.4 ± 0.1	0.5 ± 0	2.4 ± 0.1	0.4 ± 0	3.4 ± 0.2	1.1 ± 0	4.1 ± 0.2	0.6 ± 0	4.2 ± 0.1	0.8 ± 0
1335	34.57	126	27.54	18.3 ± 0.5	2.1 ± 0.1	2 ± 0.1	9.6 ± 0.2	2 ± 0.1	0.6 ± 0	3.1 ± 0.1	0.5 ± 0	4.7 ± 0.2	1.3 ± 0	5.5 ± 0.2	0.8 ± 0	5.9 ± 0.1	1 ± 0
1535	34.60	129	27.60	20 ± 0.7	1.4 ± 0.1	2.2 ± 0.1	10.6 ± 0.3	1.9 ± 0.1	0.6 ± 0	3.5 ± 0.2	0.5 ± 0	4.9 ± 0.2	1.4 ± 0.1	5.6 ± 0.2	0.9 ± 0	6.2 ± 0.2	1.2 ± 0.1
2000	34.64	133	27.69	26.8 ± 1.1	2.6 ± 0.1	3.3 ± 0.1	14.8 ± 0.4	2.8 ± 0.1	0.9 ± 0	4.7 ± 0.2	0.7 ± 0	6.1 ± 0.4	1.7 ± 0.1	6.6 ± 0.3	1 ± 0	7.3 ± 0.2	1.4 ± 0.1
Station 020 (July 06, 2012; 9° 59′ 56.4″ S; 160° 25′ 1.2″ E; depth: 2910 m)																	
25	34.83	189	21.97	4.3 ± 0.2	3.7 ± 0.1	1 ± 0	4.7 ± 0.2	1.1 ± 0.1	0.3 ± 0	1.7 ± 0.1	0.3 ± 0	2.1 ± 0.1	0.5 ± 0	1.7 ± 0.1	0.2 ± 0	1.2 ± 0	0.2 ± 0
190	35.82	127	24.67	–	–	–	–	–	–	–	–	–	–	–	–	–	–
600	34.49	162	27.12	0 ± 0	0 ± 0	0 ± 0	0 ± 0	0 ± 0	0 ± 0	0 ± 0	0 ± 0	0 ± 0	0 ± 0	0 ± 0	0 ± 0	0 ± 0	0 ± 0
900	34.49	151	27.30	14.1 ± 0.6	1.5 ± 0.1	1.8 ± 0.1	8.2 ± 0.3	1.6 ± 0.1	0.5 ± 0	2.8 ± 0.2	0.4 ± 0	3.8 ± 0.2	1.2 ± 0	4.5 ± 0.2	0.7 ± 0	4.7 ± 0.2	0.9 ± 0
1600	34.60	133	27.60	–	–	–	–	–	–	–	–	–	–	–	–	–	–
Station 021 (July 07, 2012; 10° 0′ 46.8″ S; 160° 21′ 25.2″ E; depth: 3342 m)																	
250	35.39	127	25.76	5.6 ± 0.2	2 ± 0.1	0.9 ± 0	4.1 ± 0.1	0.7 ± 0	0.2 ± 0	1.4 ± 0.1	0.2 ± 0	1.8 ± 0.1	0.5 ± 0	1.9 ± 0.1	0.3 ± 0	1.4 ± 0	0.3 ± 0
400	34.68	140	26.86	8.2 ± 0.2	1.5 ± 0	1.1 ± 0	5.3 ± 0.1	1.1 ± 0	0.3 ± 0	1.8 ± 0.1	0.3 ± 0	2.6 ± 0.1	0.8 ± 0	2.9 ± 0.1	0.4 ± 0	2.8 ± 0.1	0.5 ± 0
550	34.49	163	27.10	10.3 ± 0.2	1.2 ± 0	1.5 ± 0	6.8 ± 0.1	1.4 ± 0	0.4 ± 0	2.4 ± 0.1	0.4 ± 0	3.4 ± 0.1	1 ± 0	3.8 ± 0.1	0.6 ± 0	3.8 ± 0.1	0.7 ± 0
2115	34.64	139	27.69	27.7 ± 0.6	2.4 ± 0.1	3.5 ± 0.1	16.5 ± 0.3	3.1 ± 0.1	1 ± 0	5.1 ± 0.2	0.8 ± 0	6.4 ± 0.2	1.8 ± 0	6.5 ± 0.2	1 ± 0	7 ± 0.1	1.3 ± 0
2625	34.68	150	27.74	26.4 ± 0.4	2.1 ± 0.1	3.4 ± 0.1	15.9 ± 0.2	2.9 ± 0.1	0.9 ± 0	5.1 ± 0.2	0.8 ± 0	6.6 ± 0.2	1.9 ± 0	6.9 ± 0.2	1.1 ± 0	7.6 ± 0.1	1.4 ± 0
3280	34.70	165	27.77	31.1 ± 2	2.7 ± 0.2	4.1 ± 0.2	19 ± 0.7	3.5 ± 0.2	1.1 ± 0.1	5.5 ± 0.4	0.8 ± 0.1	6.8 ± 0.6	1.9 ± 0.1	6.9 ± 0.6	1 ± 0.1	7.1 ± 0.3	1.3 ± 0.1
Station 029 (July 09, 2012; 11° 3′ 39.6″ S; 156° 12′ 54″ E; depth: 3856 m)																	
267	35.38	128	25.78	5.2 ± 0.2	2.2 ± 0.1	0.9 ± 0	4 ± 0.1	0.8 ± 0	0.2 ± 0	1.4 ± 0.1	0.2 ± 0	1.8 ± 0.1	0.5 ± 0	1.9 ± 0.1	0.3 ± 0	1.4 ± 0	0.3 ± 0
737	34.47	160	27.21	11.4 ± 0.4	1.9 ± 0.1	1.6 ± 0	7.2 ± 0.2	1.4 ± 0.1	0.4 ± 0	2.5 ± 0.1	0.4 ± 0	3.5 ± 0.1	1 ± 0	4 ± 0.2	0.6 ± 0	4.1 ± 0.1	0.8 ± 0
934	34.50	150	27.36	15.3 ± 0.6	3.8 ± 0.1	1.9 ± 0.1	8.6 ± 0.2	1.6 ± 0.1	0.5 ± 0	2.8 ± 0.1	0.5 ± 0	3.9 ± 0.2	1.1 ± 0	4.5 ± 0.2	0.7 ± 0	4.7 ± 0.1	0.9 ± 0
1140	34.54	139	27.45	16.2 ± 0.5	2.2 ± 0	2 ± 0	9.2 ± 0.2	1.8 ± 0.1	0.6 ± 0	3.2 ± 0.1	0.5 ± 0	4.2 ± 0.2	1.3 ± 0	4.9 ± 0.2	0.8 ± 0	5.3 ± 0.1	1 ± 0
1534	34.59	133	27.59	18.9 ± 0.7	1.3 ± 0.1	2.4 ± 0.1	11.4 ± 0.3	2.2 ± 0.1	0.7 ± 0	3.8 ± 0.2	0.6 ± 0	5.2 ± 0.3	1.5 ± 0.1	5.8 ± 0.2	0.9 ± 0	6.2 ± 0.2	1.2 ± 0.1

(*continued on next page*)

Table 2 (*continued*)

Depth	Salinity	O_2	σ_θ	La	Ce	Pr	Nd	Sm	Eu	Gd	Tb	Dy	Ho	Er	Tm	Yb	Lu
(m)	(PSU)	(μmol/kg)	(kg/m^3)	(pmol/kg)													
2999	34.70	166	27.77	27.1 ± 2	2.7 ± 0.2	3.7 ± 0.2	16.9 ± 0.9	3.2 ± 0.3	1 ± 0.1	5.1 ± 0.4	0.8 ± 0	6.5 ± 0.4	1.8 ± 0.1	6.6 ± 0.4	1 ± 0.1	6.9 ± 0.4	1.3 ± 0.1
Station 034 (July 10, 2012; 11° 27′ 7.2″ S; 154° 39′ 54″ E; depth: 2005 m)																	
40	34.93	181	22.17	4 ± 0.1	3 ± 0.1	0.9 ± 0	4.2 ± 0.1	1 ± 0	0.3 ± 0	1.7 ± 0	0.3 ± 0	2 ± 0	0.6 ± 0	1.8 ± 0	0.2 ± 0	1.3 ± 0	0.2 ± 0
180	35.66	144	24.77	3.7 ± 0.1	2.1 ± 0	0.7 ± 0	3.4 ± 0	0.7 ± 0	0.3 ± 0	1.3 ± 0	0.3 ± 0	1.7 ± 0	0.5 ± 0	1.6 ± 0.1	0.2 ± 0	1.2 ± 0	0.2 ± 0
300	35.25	156	26.08	5.8 ± 0.1	2.1 ± 0.1	1 ± 0	4.5 ± 0.1	1 ± 0	0.3 ± 0	1.6 ± 0	0.3 ± 0	2.1 ± 0.1	0.6 ± 0	2.2 ± 0.1	0.3 ± 0	1.8 ± 0	0.3 ± 0
635	34.49	183	27.00	11.8 ± 0.5	3.1 ± 0.1	1.7 ± 0	7.2 ± 0.1	1.4 ± 0.1	0.4 ± 0	2.3 ± 0.1	0.4 ± 0	3.3 ± 0.1	1 ± 0	3.7 ± 0.1	0.6 ± 0	3.5 ± 0.1	0.7 ± 0
735	34.44	179	27.16	14 ± 0.6	6.5 ± 0.2	2.1 ± 0.1	8.6 ± 0.2	1.5 ± 0.1	0.5 ± 0	2.5 ± 0.1	0.4 ± 0	3.5 ± 0.1	1.1 ± 0	4.1 ± 0.1	0.6 ± 0	4 ± 0.1	0.7 ± 0
1065	34.49	154	27.37	16.5 ± 0.6	3.5 ± 0.1	2 ± 0.1	9.3 ± 0.2	1.8 ± 0.1	0.5 ± 0	3.2 ± 0.1	0.5 ± 0	4.3 ± 0.1	1.3 ± 0	4.9 ± 0.2	0.7 ± 0	4.9 ± 0.1	0.9 ± 0
1550	34.60	136	27.60	23.6 ± 1.1	3.3 ± 0.2	3 ± 0.1	13.3 ± 0.5	2.5 ± 0.1	0.7 ± 0	4.3 ± 0.2	0.7 ± 0	5.5 ± 0.3	1.6 ± 0.1	6.3 ± 0.3	0.9 ± 0	6.6 ± 0.3	1.2 ± 0.1
1665	34.61	137	27.62	24.8 ± 0.9	[1.9 ± 0.1]	3 ± 0.1	13.8 ± 0.3	2.7 ± 0.1	0.8 ± 0	4.4 ± 0.2	0.7 ± 0	5.9 ± 0.2	1.8 ± 0.1	6.5 ± 0.2	1 ± 0	6.7 ± 0.2	1.3 ± 0
1750	34.63	136	27.65	26.3 ± 0.9	2.5 ± 0.1	3.4 ± 0.1	15 ± 0.4	3 ± 0.1	0.9 ± 0	4.7 ± 0.2	0.8 ± 0	6.1 ± 0.2	1.9 ± 0.1	6.7 ± 0.3	1 ± 0	7 ± 0.2	1.3 ± 0
1920	34.65	140	27.69	–	–	–	–	–	–	–	–	–	–	–	–	–	–
Station 036 (July 11, 2012; 11° 30′ 7.2″ S; 154° 23′ 24″ E; depth: 1168 m)																	
25	34.49	195	22.09	7 ± 0.1	7.1 ± 0.1	1.8 ± 0	8.2 ± 0.1	2 ± 0.1	0.6 ± 0	2.8 ± 0.1	0.4 ± 0	3.1 ± 0.1	0.8 ± 0	2.4 ± 0.1	0.3 ± 0	1.7 ± 0	0.3 ± 0
100	35.43	163	23.89	3.7 ± 0.1	3 ± 0	0.8 ± 0	3.9 ± 0	1 ± 0	0.3 ± 0	1.5 ± 0.1	0.2 ± 0	1.9 ± 0	0.5 ± 0	1.7 ± 0.1	0.2 ± 0	1.2 ± 0	0.2 ± 0
160	35.61	141	24.60	4.1 ± 0.1	2.8 ± 0.1	0.8 ± 0	3.8 ± 0	0.9 ± 0	0.3 ± 0	1.4 ± 0.1	0.2 ± 0	1.8 ± 0.1	0.5 ± 0	1.7 ± 0.1	0.2 ± 0	1.2 ± 0	0.2 ± 0
180	35.64	144	24.96	4.4 ± 0.1	3.1 ± 0	0.8 ± 0	3.8 ± 0	0.9 ± 0	0.3 ± 0	1.4 ± 0	0.2 ± 0	1.8 ± 0.1	0.5 ± 0	1.7 ± 0	0.2 ± 0	1.2 ± 0	0.2 ± 0
400	34.94	167	26.51	7.2 ± 0.2	1.9 ± 0.1	1.1 ± 0	5.2 ± 0.1	1.1 ± 0	0.3 ± 0	1.7 ± 0.1	0.3 ± 0	2.4 ± 0.1	0.7 ± 0	2.5 ± 0.1	0.4 ± 0	2.2 ± 0	0.4 ± 0
700	34.46	182	27.09	11.4 ± 0.4	[1.4 ± 0]	1.6 ± 0	7.2 ± 0.1	1.5 ± 0.1	0.4 ± 0	2.4 ± 0.1	0.4 ± 0	3.4 ± 0.1	1 ± 0	3.8 ± 0.1	0.6 ± 0	3.7 ± 0.1	0.7 ± 0
900	34.46	170	27.24	12.6 ± 0.4	1.4 ± 0	1.6 ± 0	7.5 ± 0.1	1.5 ± 0.1	0.5 ± 0	2.5 ± 0.1	0.4 ± 0	3.6 ± 0.1	1.1 ± 0	4.1 ± 0.1	0.6 ± 0	4.2 ± 0.1	0.8 ± 0
Station 042 (July 15, 2012; 5° 8′ 42″ S; 153° 17′ 24″ E; depth: 3081 m)																	
5	34.69	192	21.71	3.6 ± 0.2	3.1 ± 0.2	0.8 ± 0	3.9 ± 0.2	0.8 ± 0	0.3 ± 0	1.4 ± 0.1	0.2 ± 0	1.7 ± 0.1	0.5 ± 0	1.5 ± 0.1	0.2 ± 0	0.9 ± 0	0.2 ± 0
50	34.75	192	21.75	–	–	–	–	–	–	–	–	–	–	–	–	–	–
100	35.46	157	22.68	–	–	–	–	–	–	–	–	–	–	–	–	–	–
180	35.65	140	24.72	4.2 ± 0.2	2.5 ± 0.1	0.7 ± 0	3.4 ± 0.1	0.8 ± 0	0.3 ± 0	1.3 ± 0.1	0.2 ± 0	1.7 ± 0.1	0.5 ± 0	1.7 ± 0.1	0.2 ± 0	1.2 ± 0	0.2 ± 0
225	35.35	152	25.85	4.9 ± 0.2	[1.4 ± 0]	0.8 ± 0	3.8 ± 0.1	1.5 ± 0.1	0.3 ± 0	1.4 ± 0.1	0.2 ± 0	2 ± 0.1	0.5 ± 0	2 ± 0.1	0.3 ± 0	1.6 ± 0	0.3 ± 0
400	34.64	174	26.84	9.8 ± 0.2	[1.8 ± 0]	1.3 ± 0.1	6.1 ± 0.1	1.2 ± 0.1	0.4 ± 0	2.1 ± 0.1	0.3 ± 0	3 ± 0.1	0.9 ± 0	3.3 ± 0.1	0.5 ± 0	3.1 ± 0.1	0.6 ± 0
500	34.54	158	27.02	11 ± 0.3	1.7 ± 0	1.5 ± 0	6.8 ± 0.1	1.4 ± 0	0.4 ± 0	2.3 ± 0.1	0.4 ± 0	3.2 ± 0.1	1 ± 0	3.6 ± 0.2	0.6 ± 0	3.6 ± 0.1	0.7 ± 0
750	34.48	154	27.23	11.9 ± 0.3	[1.6 ± 0.1]	1.6 ± 0	7.3 ± 0.1	1.5 ± 0	0.4 ± 0	2.5 ± 0.1	0.4 ± 0	3.5 ± 0.1	1.1 ± 0	4 ± 0.1	0.6 ± 0	4.1 ± 0	0.8 ± 0
1000	34.53	137	27.41	15.8 ± 0.8	2.1 ± 0.1	2.1 ± 0.1	9.4 ± 0.3	1.9 ± 0.1	0.6 ± 0	3.2 ± 0.2	0.5 ± 0	4.5 ± 0.3	1.3 ± 0.1	5 ± 0.3	0.7 ± 0	5.1 ± 0.2	1 ± 0.1
1200	34.56	130	27.49	17.9 ± 0.6	2.8 ± 0.1	2.3 ± 0.1	10.4 ± 0.2	2 ± 0.1	0.7 ± 0	3.5 ± 0.2	0.6 ± 0	4.6 ± 0.2	1.4 ± 0.1	5.1 ± 0.2	0.8 ± 0	5.6 ± 0.1	1.1 ± 0
1550	34.61	123	27.62	24.8 ± 0.7	5.1 ± 0.1	3.2 ± 0.1	14.5 ± 0.3	2.8 ± 0.1	0.9 ± 0	4.4 ± 0.2	0.7 ± 0	5.7 ± 0.2	1.7 ± 0.1	6.1 ± 0.3	1 ± 0	6.6 ± 0.2	1.2 ± 0
1750	34.62	124	27.64	28.6 ± 0.9	4.6 ± 0.2	3.3 ± 0.1	15.8 ± 0.5	3.1 ± 0.1	1 ± 0	5.2 ± 0.2	0.8 ± 0	6.5 ± 0.2	1.8 ± 0.1	6.7 ± 0.2	1.1 ± 0	7.2 ± 0.2	1.3 ± 0
2000	34.64	126	27.68	29.1 ± 1.6	3.6 ± 0.2	3.9 ± 0.2	18 ± 0.8	3.4 ± 0.2	1.1 ± 0.1	5.7 ± 0.3	0.9 ± 0	6.8 ± 0.4	1.9 ± 0.1	7.3 ± 0.5	1.1 ± 0.1	7.7 ± 0.4	1.4 ± 0.1
2500	34.66	133	27.73	32.5 ± 2.6	4.8 ± 0.2	4.7 ± 0.3	21.8 ± 0.9	4.2 ± 0.3	1.3 ± 0.1	6.7 ± 0.4	1 ± 0.1	7.9 ± 0.6	2.2 ± 0.2	8 ± 0.6	1.3 ± 0.1	8.5 ± 0.4	1.5 ± 0.1
Station 043 (July 17, 2012; 3° 59′ 52.8″ S; 155° 35′ 38.4″ E; depth: 1925 m)																	
5	34.66	191	21.72	3.6 ± 0.2	2.8 ± 0.2	0.7 ± 0	3.5 ± 0.1	0.7 ± 0	0.2 ± 0	1.3 ± 0.1	0.2 ± 0	1.6 ± 0.1	0.5 ± 0	1.4 ± 0.1	0.2 ± 0	0.8 ± 0	0.1 ± 0
150	35.91	138	23.99	4.5 ± 0.1	2.6 ± 0.1	0.8 ± 0	3.7 ± 0.1	0.7 ± 0	0.2 ± 0	1.3 ± 0.1	0.2 ± 0	1.7 ± 0.1	0.5 ± 0	1.7 ± 0.1	0.2 ± 0	1.2 ± 0	0.2 ± 0
230	35.16	99	26.14	[25.5 ± 0.8]	[12.3 ± 0.3]	[1.2 ± 0]	[5.2 ± 0.1]	[0.9 ± 0]	[0.3 ± 0]	[1.6 ± 0.1]	[0.3 ± 0]	[2.2 ± 0.1]	[0.6 ± 0]	[2.3 ± 0.1]	[0.3 ± 0]	[2.1 ± 0]	[0.4 ± 0]
700	34.51	128	27.18	13.1 ± 0.3	1.8 ± 0	1.7 ± 0	7.6 ± 0.1	1.5 ± 0	0.5 ± 0	2.5 ± 0.1	0.4 ± 0	3.4 ± 0.1	1.1 ± 0	4 ± 0.1	0.6 ± 0	4.2 ± 0.1	0.8 ± 0
1200	34.56	105	27.47	16.4 ± 0.5	1.9 ± 0	2.1 ± 0	9.6 ± 0.2	1.9 ± 0.1	0.6 ± 0	3.2 ± 0.1	0.5 ± 0	4.4 ± 0.1	1.3 ± 0	4.9 ± 0.2	0.8 ± 0	5.5 ± 0.1	1 ± 0
Station 046 (July 18, 2012; 4° 42′ 0″ S; 154° 52′ 48″ E; depth: 3117 m)																	
50	34.79	190	21.85	3.6 ± 0.1	2.2 ± 0.1	0.7 ± 0	3.3 ± 0	0.7 ± 0	0.2 ± 0	1.3 ± 0	0.2 ± 0	1.5 ± 0	0.4 ± 0	1.4 ± 0	0.2 ± 0	0.8 ± 0	0.1 ± 0
150	35.97	129	23.97	3.5 ± 0.1	1.3 ± 0	0.6 ± 0	2.6 ± 0	0.6 ± 0	0.2 ± 0	1.1 ± 0	0.2 ± 0	1.5 ± 0	0.4 ± 0	1.5 ± 0	0.2 ± 0	1 ± 0	0.2 ± 0
400	34.65	124	26.89	11.3 ± 0.3	2.5 ± 0.1	1.4 ± 0	6.5 ± 0.1	1.3 ± 0.1	0.4 ± 0	2.1 ± 0.1	0.4 ± 0	3 ± 0.1	0.9 ± 0	3.4 ± 0.1	0.5 ± 0	3.3 ± 0.1	0.6 ± 0
700	34.54	89	27.19	12.5 ± 0.3	0.9 ± 0	1.6 ± 0	7.2 ± 0.2	1.4 ± 0.1	0.5 ± 0	2.5 ± 0.1	0.4 ± 0	3.5 ± 0.1	1 ± 0	4 ± 0.1	0.6 ± 0	4.1 ± 0.1	0.8 ± 0
1000	34.54	112	27.39	15.6 ± 0.5	2 ± 0.1	1.9 ± 0	8.9 ± 0.2	1.8 ± 0.1	0.5 ± 0	3.1 ± 0.1	0.5 ± 0	4.2 ± 0.1	1.2 ± 0	4.7 ± 0.1	0.7 ± 0	4.9 ± 0.1	0.9 ± 0
Station 047 (July 18, 2012; 4° 56′ 2.4″ S; 154° 38′ 52.8″ E; depth: 1004 m)																	
25	34.67	190	21.78	4.4 ± 0.1	3.3 ± 0.1	1 ± 0	4.4 ± 0.1	1 ± 0	0.3 ± 0	1.6 ± 0	0.2 ± 0	1.9 ± 0.1	0.5 ± 0	1.6 ± 0	0.2 ± 0	1 ± 0	0.2 ± 0
156	36.02	126	24.41	4.6 ± 0.1	2.6 ± 0	0.6 ± 0	3 ± 0	0.6 ± 0	0.2 ± 0	1.2 ± 0	0.2 ± 0	1.6 ± 0	0.5 ± 0	1.7 ± 0	0.2 ± 0	1.2 ± 0	0.2 ± 0

(*continued on next page*)

Table 2 (*continued*)

Depth	Salinity	O_2	σ_θ	La	Ce	Pr	Nd	Sm	Eu	Gd	Tb	Dy	Ho	Er	Tm	Yb	Lu
(m)	(PSU)	(μmol/kg)	(kg/m^3)	(pmol/kg)													
264	35.08	106	26.27	[7.4 ± 0.1]	1.7 ± 0	1.1 ± 0	4.8 ± 0.1	0.9 ± 0	0.3 ± 0	1.6 ± 0.1	0.3 ± 0	2.2 ± 0.1	0.7 ± 0	2.4 ± 0.1	0.3 ± 0	2.1 ± 0	0.4 ± 0
635	34.52	129	27.20	13.3 ± 0.3	2.6 ± 0.2	1.7 ± 0	7.7 ± 0.1	1.5 ± 0	0.5 ± 0	2.6 ± 0.1	0.4 ± 0	3.6 ± 0.2	1.1 ± 0	4.1 ± 0.1	0.7 ± 0	4.2 ± 0.1	0.8 ± 0
Station 053 (July 19, 2012; 4° 54′ 18″ S; 152° 52′ 12″ E; depth: 733 m)																	
25	34.88	189	21.99	4.9 ± 0.2	4.1 ± 0.2	1.2 ± 0.1	5.7 ± 0.3	1.4 ± 0.1	0.5 ± 0	2.1 ± 0.1	0.3 ± 0	2.5 ± 0.1	0.7 ± 0	2.1 ± 0.1	0.3 ± 0	1.5 ± 0.1	0.2 ± 0
149	35.61	142	24.72	6.3 ± 0.2	5.2 ± 0.1	0.9 ± 0	4 ± 0.1	0.9 ± 0	0.3 ± 0	1.5 ± 0.1	0.2 ± 0	1.8 ± 0.1	0.5 ± 0	1.7 ± 0	0.2 ± 0	1.2 ± 0	0.2 ± 0
335	34.98	161	26.45	[7.6 ± 0.1]	1.8 ± 0	1.2 ± 0	5.3 ± 0.1	1.1 ± 0	0.3 ± 0	1.8 ± 0.1	0.3 ± 0	2.5 ± 0.1	0.7 ± 0	2.6 ± 0.1	0.4 ± 0	2.3 ± 0	0.4 ± 0
719	34.48	158	27.22	[12.6 ± 0.5]	1.5 ± 0	1.7 ± 0	7.8 ± 0.1	1.5 ± 0	0.5 ± 0	2.6 ± 0.1	0.4 ± 0	3.7 ± 0.1	1.1 ± 0	4.2 ± 0.1	0.6 ± 0	4.2 ± 0.1	0.8 ± 0
Station 056 (July 20, 2012; 4° 4′ 37.2″ S; 152° 32′ 20.4″ E; depth: 1580 m)																	
1582	34.60	125	27.59	23.4 ± 0	3.8 ± 0	3.1 ± 0	14.3 ± 0	2.8 ± 0	0.8 ± 0	4.8 ± 0	0.7 ± 0	5.9 ± 0	1.8 ± 0	6.6 ± 0	0.9 ± 0	6.7 ± 0	1.2 ± 0
Station 057 (July 20, 2012; 4° 34′ 12″ S; 152° 31′ 22.8″ E; depth: 2552 m)																	
25	34.77	192	21.91	4.1 ± 0.1	3.5 ± 0.1	1 ± 0	5.2 ± 0.1	1.3 ± 0.1	0.5 ± 0	2.1 ± 0.1	0.3 ± 0	2.3 ± 0.1	0.6 ± 0	2 ± 0.1	0.3 ± 0	1.3 ± 0	0.2 ± 0
150	35.58	139	24.20	3.8 ± 0.2	2.6 ± 0.1	0.8 ± 0	3.7 ± 0.1	0.9 ± 0.1	0.3 ± 0	1.4 ± 0.1	0.2 ± 0	1.8 ± 0.1	0.5 ± 0	1.7 ± 0.1	0.2 ± 0	1.2 ± 0	0.2 ± 0
250	35.27	152	26.00	5.4 ± 0.2	2.1 ± 0.1	0.9 ± 0.1	4.2 ± 0.1	0.9 ± 0.1	0.3 ± 0	1.5 ± 0.1	0.2 ± 0	2 ± 0.1	0.6 ± 0	2.1 ± 0.1	0.3 ± 0	1.7 ± 0	0.3 ± 0
450	34.65	171	26.85	9.3 ± 0.2	1.5 ± 0	1.3 ± 0	6.2 ± 0.1	1.2 ± 0.1	0.4 ± 0	2.1 ± 0.1	0.3 ± 0	2.9 ± 0.1	0.9 ± 0	3.1 ± 0.1	0.5 ± 0	3.1 ± 0	0.6 ± 0
580	34.51	177	27.02	12.1 ± 0.3	2.5 ± 0.1	1.5 ± 0	6.8 ± 0.1	1.3 ± 0	0.4 ± 0	2.2 ± 0.1	0.4 ± 0	3.1 ± 0.1	0.9 ± 0	3.6 ± 0.1	0.5 ± 0	3.6 ± 0.1	0.7 ± 0
850	34.50	143	27.33	13.7 ± 0.4	1.6 ± 0	1.7 ± 0	8.1 ± 0.2	1.6 ± 0.1	0.5 ± 0	2.9 ± 0.1	0.5 ± 0	3.9 ± 0.1	1.2 ± 0	4.4 ± 0.1	0.7 ± 0	4.8 ± 0.1	0.9 ± 0
1302	34.57	129	27.51	19.2 ± 0.5	2.8 ± 0.1	2.4 ± 0.1	11.5 ± 0.3	2.2 ± 0.1	0.7 ± 0	3.9 ± 0.2	0.6 ± 0	5.1 ± 0.2	1.5 ± 0	5.5 ± 0.2	0.9 ± 0	6 ± 0.1	1.1 ± 0
1650	34.61	124	27.62	–	–	–	–	–	–	–	–	–	–	–	–	–	–
2201	34.65	135	27.71	31.2 ± 0.9	3.5 ± 0.1	4.2 ± 0.1	20 ± 0.5	3.9 ± 0.2	1.3 ± 0	6.3 ± 0.3	1 ± 0	7.9 ± 0.3	2.1 ± 0	7.7 ± 0.2	1.2 ± 0	8.2 ± 0.2	1.5 ± 0
Station 058 (July 21, 2012; 5° 30′ 10.8″ S; 152° 5′ 52.8″ E; depth: 1142 m)																	
215	35.50	135	25.51	4.8 ± 0.2	2.2 ± 0.1	0.8 ± 0	3.9 ± 0.1	0.8 ± 0	0.3 ± 0	1.4 ± 0.1	0.2 ± 0	1.8 ± 0.1	0.5 ± 0	1.8 ± 0.1	0.3 ± 0	1.4 ± 0	0.2 ± 0
1100	34.55	133	27.47	18.9 ± 0.7	3.1 ± 0.1	2.3 ± 0.1	11 ± 0.3	2.2 ± 0.1	0.7 ± 0	3.7 ± 0.2	0.6 ± 0	4.9 ± 0.2	1.4 ± 0.1	5.4 ± 0.2	0.8 ± 0	5.7 ± 0.2	1 ± 0
Station 060 (July 22, 2012; 6° 10′ 1.2″ S; 152° 29′ 49.2″ E; depth: 5609 m)																	
35	34.74	193	22.19	5 ± 0.1	4.5 ± 0.1	1.1 ± 0	5.3 ± 0.1	1.2 ± 0	0.4 ± 0	1.8 ± 0.1	0.3 ± 0	2.1 ± 0.1	0.6 ± 0	1.8 ± 0.1	0.2 ± 0	1.2 ± 0	0.2 ± 0
180	35.73	135	24.70	4.2 ± 0.2	2.3 ± 0.1	0.7 ± 0	3.4 ± 0.1	0.7 ± 0	0.2 ± 0	1.2 ± 0.1	0.2 ± 0	1.6 ± 0.1	0.5 ± 0	1.6 ± 0.1	0.2 ± 0	1.1 ± 0	0.2 ± 0
250	35.33	124	25.86	7.4 ± 0.1	3.7 ± 0.1	1 ± 0	4.9 ± 0.1	1 ± 0	0.3 ± 0	1.6 ± 0.1	0.2 ± 0	2 ± 0.1	0.6 ± 0	2.2 ± 0.1	0.3 ± 0	1.7 ± 0	0.3 ± 0
480	34.53	173	27.03	11.2 ± 0.3	2.6 ± 0.1	1.5 ± 0.1	6.8 ± 0.1	1.3 ± 0.1	0.4 ± 0	2.3 ± 0.1	0.4 ± 0	3.1 ± 0.1	1 ± 0	3.5 ± 0.1	0.6 ± 0	3.6 ± 0.1	0.7 ± 0
1000	34.53	138	27.43	16.3 ± 0.3	2.7 ± 0.1	2 ± 0	9.4 ± 0.1	1.8 ± 0.1	0.6 ± 0	3 ± 0.1	0.5 ± 0	4 ± 0.1	1.3 ± 0	4.8 ± 0.2	0.7 ± 0	5 ± 0.1	1 ± 0
1600	34.61	124	27.62	23.9 ± 0.9	5 ± 0.2	3.2 ± 0.1	14.5 ± 0.3	2.8 ± 0.1	0.9 ± 0	4.6 ± 0.2	0.7 ± 0	5.8 ± 0.2	1.8 ± 0	6.2 ± 0.2	1 ± 0	6.8 ± 0.1	1.3 ± 0
1800	34.63	125	27.67	28.4 ± 0.6	7.8 ± 0.2	3.9 ± 0.1	18.1 ± 0.3	3.4 ± 0.1	1.1 ± 0	5.4 ± 0.2	0.8 ± 0	6.8 ± 0.3	1.9 ± 0.1	7 ± 0.2	1.1 ± 0	7.4 ± 0.2	1.4 ± 0
2541	34.66	132	27.73	35.4 ± 1	3.5 ± 0.1	5.1 ± 0.1	23.8 ± 0.5	4.6 ± 0.2	1.5 ± 0	7 ± 0.3	1.1 ± 0	8.6 ± 0.4	2.3 ± 0.1	8.1 ± 0.4	1.3 ± 0.1	8.7 ± 0.2	1.6 ± 0.1
3250	34.69	155	27.76	41.1 ± 1.1	5.8 ± 0.2	6.1 ± 0.2	28.1 ± 0.6	5.3 ± 0.2	1.7 ± 0	8 ± 0.3	1.2 ± 0	9.1 ± 0.4	2.6 ± 0.1	8.3 ± 0.3	1.4 ± 0	8.9 ± 0.2	1.6 ± 0.1
4000	34.70	158	27.77	41 ± 1.4	5.6 ± 0.2	6.3 ± 0.2	28.8 ± 0.8	5.9 ± 0.2	1.8 ± 0.1	8.2 ± 0.3	1.2 ± 0	9.5 ± 0.3	2.5 ± 0.1	8.7 ± 0.3	1.3 ± 0	8.9 ± 0.2	1.6 ± 0.1
4500	34.70	160	27.77	41.9 ± 1.6	8 ± 0.3	6.8 ± 0.3	30.2 ± 1	6 ± 0.3	1.9 ± 0.1	8.4 ± 0.5	1.3 ± 0.1	9.6 ± 0.6	2.6 ± 0.1	8.8 ± 0.5	1.4 ± 0.1	8.9 ± 0.3	1.6 ± 0.1
4750	34.70	160	27.77	47.3 ± 1	14.6 ± 0.3	7 ± 0.2	30.4 ± 0.4	5.6 ± 0.2	1.8 ± 0	7.8 ± 0.3	1.2 ± 0	8.9 ± 0.4	2.4 ± 0.1	8.4 ± 0.3	1.2 ± 0	8.3 ± 0.1	1.6 ± 0
5000	34.70	161	27.77	39.3 ± 0.9	5.3 ± 0.1	5.4 ± 0.1	25.4 ± 0.3	4.8 ± 0.2	1.5 ± 0	7 ± 0.2	1.1 ± 0	8.1 ± 0.3	2.3 ± 0.1	8 ± 0.3	1.2 ± 0	7.8 ± 0.1	1.5 ± 0
5603	34.70	162	27.77	41.2 ± 1.5	5.6 ± 0.2	6 ± 0.2	26.3 ± 0.7	4.9 ± 0.2	1.4 ± 0.1	6.8 ± 0.4	1 ± 0.1	8 ± 0.4	2.2 ± 0.1	7.6 ± 0.4	1.1 ± 0.1	7.6 ± 0.2	1.4 ± 0
Station 071 (July 25, 2012; 8° 19′ 55.2″ S; 151° 17′ 27.6″ E; depth: 1563 m)																	
50	34.80	192	22.39	3.8 ± 0.3	[2.6 ± 0.2]	0.8 ± 0.1	4 ± 0.2	1 ± 0.1	0.3 ± 0	1.5 ± 0.1	0.2 ± 0	1.8 ± 0.1	0.5 ± 0	1.7 ± 0.1	0.2 ± 0	1.1 ± 0	0.2 ± 0
160	35.66	138	24.60	4.6 ± 0.3	5.9 ± 0.4	0.8 ± 0	3.9 ± 0.2	0.7 ± 0.1	0.2 ± 0	1.3 ± 0.1	0.2 ± 0	1.7 ± 0.1	0.5 ± 0	1.7 ± 0.1	0.2 ± 0	1.2 ± 0.1	0.2 ± 0
400	34.98	165	26.47	7.9 ± 0.6	4.6 ± 0.2	1.1 ± 0.1	5.2 ± 0.2	1.1 ± 0.1	0.3 ± 0	1.8 ± 0.1	0.3 ± 0	2.5 ± 0.2	0.7 ± 0	2.5 ± 0.1	0.4 ± 0	2.2 ± 0.1	0.4 ± 0
600	34.49	178	27.06	12 ± 0.9	[1.9 ± 0.2]	1.5 ± 0.1	6.9 ± 0.4	1.3 ± 0.1	0.4 ± 0	2.3 ± 0.2	0.4 ± 0	3.3 ± 0.3	1 ± 0.1	3.7 ± 0.2	0.6 ± 0	3.7 ± 0.2	0.7 ± 0.1
1100	34.52	143	27.41	32.3 ± 1.2	5.6 ± 0.2	2.1 ± 0.1	9.7 ± 0.2	1.9 ± 0.1	0.6 ± 0	3.2 ± 0.1	0.5 ± 0	4.3 ± 0.2	1.3 ± 0	4.9 ± 0.2	0.8 ± 0	5.2 ± 0.1	1 ± 0
Station 073 - Filtrated (July 26, 2012; 7° 9′ 57.6″ S; 149° 59′ 56.4″ E; depth: 5253 m)																	
50	35.06	171	22.66	4 ± 0.1	3.1 ± 0.1	0.9 ± 0	4.1 ± 0.1	0.9 ± 0	0.3 ± 0	1.5 ± 0.1	0.2 ± 0	1.9 ± 0.1	0.5 ± 0	1.7 ± 0.1	0.2 ± 0	1.2 ± 0	0.2 ± 0
170	35.59	141	24.76	4 ± 0.2	2.5 ± 0.1	0.8 ± 0	3.6 ± 0.1	0.7 ± 0	0.2 ± 0	1.4 ± 0.1	0.2 ± 0	1.8 ± 0.1	0.5 ± 0	1.6 ± 0.1	0.2 ± 0	1.2 ± 0	0.2 ± 0
200	35.60	140	24.90	3.6 ± 0.1	[1.6 ± 0.1]	0.7 ± 0	3.3 ± 0.1	0.7 ± 0	0.2 ± 0	1.3 ± 0.1	0.2 ± 0	1.7 ± 0.1	0.5 ± 0	1.7 ± 0.1	0.2 ± 0	1.2 ± 0	0.2 ± 0
700	34.47	169	27.16	11.2 ± 0.2	1.2 ± 0	1.5 ± 0	7.1 ± 0.1	1.4 ± 0	0.5 ± 0	2.4 ± 0.1	0.4 ± 0	3.5 ± 0.1	1 ± 0	4 ± 0.1	0.6 ± 0	4 ± 0.1	0.7 ± 0
1650[a]	*34.61*	*123*	*27.62*	*19.6 ± 0.9*	*2.2 ± 0.2*	*2.5 ± 0*	*11.7 ± 0.2*	*2.3 ± 0.1*	*0.7 ± 0*	*3.8 ± 0*	*0.6 ± 0*	*4.8 ± 0.1*	*1.4 ± 0*	*5.2 ± 0*	*0.8 ± 0*	*5.6 ± 0.1*	*1.1 ± 0*

(*continued on next page*)

Table 2 (*continued*)

Depth	Salinity	O_2	σ_θ	La	Ce	Pr	Nd	Sm	Eu	Gd	Tb	Dy	Ho	Er	Tm	Yb	Lu
(m)	(PSU)	(μmol/kg)	(kg/m^3)	(pmol/kg)													
Station 077 (July 28, 2012; 5° 57′ 3.6″ S; 147° 39′ 36″ E; depth: 1045 m)																	
25	34.77	191	22.35	9.1 ± 0.2	3.7 ± 0.1	1 ± 0	4.9 ± 0.1	1.1 ± 0	0.4 ± 0	1.8 ± 0.1	0.3 ± 0	2.2 ± 0.1	0.6 ± 0	1.8 ± 0	0.2 ± 0	1.3 ± 0	0.2 ± 0
180	35.61	140	24.85	3.9 ± 0.1	2.3 ± 0	0.7 ± 0	3.4 ± 0	0.8 ± 0	0.2 ± 0	1.3 ± 0	0.2 ± 0	1.7 ± 0	0.5 ± 0	1.6 ± 0	0.2 ± 0	1.1 ± 0	0.2 ± 0
501	34.57	178	26.94	13.2 ± 0.2	5.2 ± 0.5	1.8 ± 0	8 ± 0.1	1.6 ± 0	0.5 ± 0	2.4 ± 0.1	0.4 ± 0	3.3 ± 0.1	1 ± 0	3.6 ± 0.1	0.5 ± 0	3.6 ± 0.1	0.6 ± 0
701	34.48	159	27.20	13.1 ± 0.2	[1.6 ± 0]	1.7 ± 0	7.9 ± 0.1	1.5 ± 0	0.5 ± 0	2.7 ± 0.1	0.4 ± 0	3.7 ± 0.1	1.1 ± 0	4.3 ± 0.1	0.7 ± 0	4.3 ± 0.1	0.8 ± 0
983	34.51	145	27.35	20 ± 0.7	2.9 ± 0.1	2.1 ± 0	9.6 ± 0.2	1.9 ± 0.1	0.6 ± 0	3.1 ± 0.1	0.5 ± 0	4.3 ± 0.2	1.3 ± 0	4.8 ± 0.1	0.8 ± 0	5 ± 0.1	1 ± 0
Station 082- non-filtrated (August 03, 2012; 13° 59′ 49.2″ S; 156° 0′ 25.2″ E; depth: 2586 m)																	
25	34.93	197	22.92	6.6 ± 0.2	4.9 ± 0.1	0.9 ± 0	4.2 ± 0.1	0.9 ± 0.1	0.4 ± 0	1.7 ± 0.1	0.2 ± 0	1.9 ± 0.1	0.5 ± 0	1.7 ± 0.1	0.2 ± 0	1.1 ± 0	0.2 ± 0
180	35.79	129	24.65	6.2 ± 0.3	4.6 ± 0.2	0.8 ± 0	3.5 ± 0.1	0.8 ± 0	0.2 ± 0	1.3 ± 0.1	0.2 ± 0	1.6 ± 0.1	0.5 ± 0	1.6 ± 0.1	0.2 ± 0	1.1 ± 0	0.2 ± 0
700	34.47	165	27.13	14 ± 0.6	4.5 ± 0.2	1.9 ± 0.1	8.1 ± 0.2	1.6 ± 0.1	0.5 ± 0	2.9 ± 0.1	0.4 ± 0	3.8 ± 0.2	1.1 ± 0	4.3 ± 0.2	0.7 ± 0	4.1 ± 0.1	0.7 ± 0
800	34.45	163	27.23	15.5 ± 0.7	4.4 ± 0.2	2 ± 0.1	8.6 ± 0.3	1.7 ± 0.1	0.5 ± 0	2.9 ± 0.1	0.5 ± 0	3.9 ± 0.2	1.2 ± 0.1	4.6 ± 0.2	0.7 ± 0	4.5 ± 0.1	0.8 ± 0
1000	34.50	151	27.38	17.3 ± 0.7	14 ± 0.3	2.1 ± 0.1	9.5 ± 0.2	1.8 ± 0.1	0.6 ± 0	3.3 ± 0.1	0.5 ± 0	4.2 ± 0.1	1.3 ± 0.1	4.9 ± 0.2	0.8 ± 0	5 ± 0.1	0.9 ± 0
1200[a]	*34.54*	*145*	*27.48*	*20 ± 1.7*	*6.9 ± 3*	*2.2 ± 0*	*10 ± 0.2*	*1.9 ± 0.1*	*0.6 ± 0*	*3.3 ± 0*	*0.5 ± 0*	*4.6 ± 0.1*	*1.4 ± 0*	*5.3 ± 0.1*	*0.8 ± 0*	*5.6 ± 0.1*	*1.1 ± 0*
1350	34.57	140	27.53	22.1 ± 1.2	3 ± 0.1	2.4 ± 0.1	11 ± 0.4	2.3 ± 0.1	0.6 ± 0	3.7 ± 0.2	0.6 ± 0	5.1 ± 0.3	1.5 ± 0.1	5.8 ± 0.3	0.9 ± 0	6 ± 0.2	1.2 ± 0.1
2000	34.64	141	27.67	29.1 ± 1.1	10.7 ± 0.4	3.6 ± 0.1	14.5 ± 0.4	2.7 ± 0.2	0.9 ± 0.1	4.7 ± 0.2	0.7 ± 0	6.1 ± 0.2	1.8 ± 0.1	6.8 ± 0.3	1 ± 0	7.3 ± 0.2	1.5 ± 0.1

Square brackets indicate data with low recoveries.
[a] Italic values refer to data with its statistical error bar.

Three main processes could condition the distribution of the REE in the Solomon Sea: 1) advection of waters from outside already displaying such vertical shape, consistent with the surface-scavenging and depth-dissolution hypothesis characterizing the fate of these elements along the general circulation (De Baar et al., 1985a; Elderfield et al., 1988; Garcia-Solsona et al., 2014; Sholkovitz et al., 1994; Takebe, 2005); 2) external inputs as for example dissolved or solid material weathered from the surrounding islands or dust of volcanic origin and 3) internal processes specific of this area. Disentangling properly the respective roles of these three processes would require the quantification of the first term by performing an analysis such as the Optimum Multiparameter Analysis (OMP; Tomczak and Large, 1989). Such a method would ideally allow identifying profiles as mixing of a few water types sources, by assuming that parameters such as nutrients and oxygen are conservative. Although promising, this method would be very uncertain in this region and would require significant additional work. Indeed, the Solomon Sea is characterized by a highly variable and complex dynamic, important diapycnal mixing (Germineaud et al., 2016), by water masses sources that are not easily identifiable (Gasparin et al., 2014), and high diazotrophic blooms that question the assumption of conservative parameters (Ganachaud et al., 2017). Therefore, we choose to apply a simple box model to estimate the dNd and dREE enrichments within the Solomon Sea (see Section 5.1).

In any case, beyond the observed general concentration increase, the vertical shape of the profiles shows subtle but interesting variations:

- Down to 3000 m, all the concentrations linearly increase, although the dYb profile is always slightly more convex than the 3 other dREE ones;
- In the southern part of our study (Coral Sea and Solomon Sea entrance, Fig. 3a), a break is observed in the linearity at 3000 m, with dREE concentration values slightly lower between 3000 and 4000 m. In the northern and almost deepest part of the Solomon Sea, at station 60, dREE profiles show a local maximum between 4000 and 5000 m, dREE concentrations being maximal in this layer and then decreasing toward the bottom. The convex shape of dYb is more pronounced at this station (Fig. 3c). This particular shape could be related to the fact that the Solomon Sea is considered as a sealed area below 3000–3500 m, separated from the outer world by islands and sills (Germineaud, 2016; Sokolov and Rintoul, 2000). This topographic constraint might increase the residence time of the waters at these depths, facilitating the scavenging to operate and yielding the slight depletion observed in the deepest part of the profiles;
- On average, dREE concentrations are slightly enriched within the Solomon Sea compared to the sites located outside of it. For example, dNd average value is of ~3.5 pmol/kg in the Solomon Sea for the isopycnal layer 24 kg/m^3 $< \sigma_\theta <$ 26 kg/m^3 while of 2.5 pmol/kg for the same density layer in the Coral Sea and east of the Solomon archipelago (see station 04, 10, 34 and 71, Fig. 3).
- Fig. 3e shows a slight maximum at station 21, suggesting an input of Solomon Archipelago material into seawater passing through Indispensable Strait.

In addition to these features affecting the profiles, local enrichments are observed at specific stations and depths such as at the surface of stations 36, 57 and 77, very likely reflecting the proximity between these stations and the coast. Within the thermocline some layers also show enriched dREE concentrations (e.g. around 500 m at station 42, 46, 57, 77; in the intermediate waters, around 700 m, at station 13, 21, 34; at 980 m at station 29).

Dissolved cerium (dCe) concentrations are reported in Table 1 and some data will be shown later as part of the discussion. As often observed in seawater where the oxidized Ce(IV) is poorly soluble and then behaves differently to the remaining trivalent REEs, dCe shows a reverse behavior compared to the other dREEs, with high concentrations

Table 3
Average dNd concentration (pmol/Kg) in the different layers of the box model.

Water mass	Upper σ_θ (kg/m^3)	Station 34	Station 29	Station 77	Station 57	Station 42
Upper thermocline water (UTW)	24–25.3	0.49 ± 0.01	0.51 ± 0.05	0.49 ± 0.01	0.54 ± 0.02	0.50 ± 0.01
Lower thermocline water (LTW)	25.3–26.9	0.65 ± 0.01	0.57 ± 0.02	1.15 ± 0.01	0.75 ± 0.20	0.72 ± 0.24
Intermediate water (IW)	26.9–27.4	1.21 ± 0.16	1.15 ± 0.14	1.22 ± 0.14	1.08 ± 0.13	1.13 ± 0.20
Upper Circumpolar Deep Water (UCDW) - upper extent	27.4–26.65	2.02 ± 0.12	1.48 ± 0.22	–	1.65 ± 0.04	1.96 ± 0.40
Upper Circumpolar Deep Water (UCDW) - lower extent	27.65–27.76	–	2.44 ± 0.12	–	2.89 ± 0.08	2.87 ± 0.38

at the top of the water column, decreasing at intermediate levels before increasing again slightly in the deep and bottom waters due to its preference for scavenging (see station 29, 42, 71 and 73, Table 1; De Baar et al., 1983; De Baar et al., 1985a; Elderfield et al., 1988; Goldberg et al., 1963; Liu et al., 1988; Piepgras and Jacobsen, 1992; Sholkovitz et al., 1994; Tachikawa et al., 1999). However, consistently with the other dREEs, dCe maxima are observed at some specific locations: in surface layers at station 36 and 77, close to the surface and at 735 m at station 34 and slightly deeper (934 m) at station 29 (Table 1).

4.2. Comparison with previous studies

Two previous studies analyzed samples outside the Solomon Sea and in the Coral Sea (Grenier et al., 2013; Zhang and Nozaki, 1996), allowing us to compare our data with published values. Fig. 4 shows the locations of these stations and the dREE concentrations versus potential density in order to compare the dREE values in the same isopycnal layers. This figure highlights the excellent agreement between our data and these previous results. The minor difference observed between the surface dLa concentrations at SA-7 and at station 82 of our study likely reflects the dissimilarity in our sampling locations and times of the year, in this region of high eddy variability (Keppler et al., 2018).

In Vitiaz Strait, a striking similarity between our results (station 77) and those of Grenier et al. (2013, their station EUC-30) is also observed, despite the difference in sampling times in this highly variable and turbulent region (Fig. 4). This strait is narrow and relatively shallow (1200 m deep) in comparison with Solomon Sea average depth; the continental influence on dREE concentrations is therefore suggested to be high in such location. This constancy of concentration could suggest that the REE concentrations are “buffered” by interplay of different external and internal processes.

4.3. Dissolved REE patterns

Fractionation of the dREEs from each other during oceanic processes (such as particulate scavenging, remineralization, or fresh continental weathering) could be identified using the normalization of dREE concentrations in seawater to those contained in shale, a material representing the average crustal geochemical composition. Here we used the Post-Archean Australian Shale or “PAAS” (McLennan, 1989). The PAAS-normalized REE patterns are presented in Fig. 5.

The main characteristics of the dREE patterns observed in the Coral and Solomon Seas are consistent with those found in the literature: the obvious negative dCe anomalies reflect the impact of the poor solubility and preferential scavenging of this element. The (dNd_n/dYb_n) ratio, which informs about the dLREE versus dHREE slope evolution, is maximum in surface, decreasing from ~0.3 to approximately 0.1 at intermediate level (~1000 m), from where it increases again in the deep and bottom waters. These observations agree with previously published results (Bertram and Elderfield, 1993; De Baar et al., 1985a; Tachikawa et al., 1999; Garcia-Solsona et al., 2014; Grenier et al., 2013, 2018; Zhang and Nozaki, 1996).

dREE patterns are relatively flat in surface waters, which indicates that recent –maybe still ongoing– lithogenic inputs affected these upper layers. The evolution of the pattern shapes with depth reflects the differential scavenging along the water column. A slight local maximum is often observed for the dMREEs, as already noticed by Grenier et al. (2013) in the same area.

5. Discussion

5.1. Nd and dREE enrichments within the Solomon Sea

A simple box model was built for the Solomon Sea, allowing us to estimate the dREE budget for different isopycnal layers between its southern entrance (southern section) and its northern exits (Vitiaz Strait, St George's Channel and Solomon Strait). The box model proposed here aims at identifying whether dREE concentrations get enriched, depleted, or stay constant while crossing the Solomon Sea and estimating the associated net fluxes (positive if inputs dominate, negative if outputs dominate, null if inputs and outputs are equivalent). Here we discuss more specifically the Nd budget, results for all the REEs are compiled in Table A in the supplementary material. Further developments that will include the ongoing measurements of Nd isotopic compositions will allow a better quantification of exchange processes, if any. The scheme of the box model is proposed in Fig. 6. This box model is applied to the upper thermocline layer (σ_θ = 24–25.3 kg/m^3), the lower thermocline layer (σ_θ = 25.3–26.9 kg/m^3), the intermediate waters (σ_θ = 26.9–27.4 kg/m^3), and the deeper UCDW waters (σ_θ = 27.4–27.65 and 27.65–27.76 kg/m^3). We also performed the same calculation on a unique box comprising the thermocline and intermediate layers (σ_θ = 24–27.4 kg/m^3) in order to reveal the enrichment/depletion of dREEs throughout the water column (see Table A in the supplementary material). The lack of water mass transport data for the deep waters prevents us to build the box model down to the bottom (see Table 4).

Our box model considers the Solomon Sea as a closed area at steady state and assumes that incoming and exiting water fluxes are balanced (Fig. 6a). Two upstream sources (incoming NGCU and direct NVJ) are feeding the Solomon Sea across the southern entrance and three downstream fluxes (SGU, NICU and NGCU) are exiting from it through the different straits (NGCU through Vitiaz Strait, SGU through St George's Channel, NICU through Solomon Strait). The required parameters to achieve the model calculation are the water mass transports and the Nd concentrations of each layer. Water flowing equatorward into the Solomon Sea includes the transports of the NGCU (W_E), and of the direct inflow (W_N). Meanwhile, water leaving the Solomon Sea gathers the water fluxes exiting through Solomon Strait (W_S), St. George's Strait (W_G) and Vitiaz Strait (W_V). Respective dissolved Nd concentrations considered here are Nd_E, Nd_N at the southern entrance and Nd_S, Nd_G and Nd_V at the northern exits (Fig. 6a and b). Under the hypothesis that diapycnal mixing is weak in this area, we obtain, for each density layer, the following equation:

$$W_E \cdot [Nd]_E + W_N \cdot [Nd]_N + F_{tot\ PANDORA} = W_S \cdot [Nd]_S + W_G \cdot [Nd]_G + W_V \cdot [Nd]_V \quad (1)$$

where $F_{tot\ PANDORA}$ is the total net flux into seawater from the surrounding coasts.

The transports are computed for each density layer using the

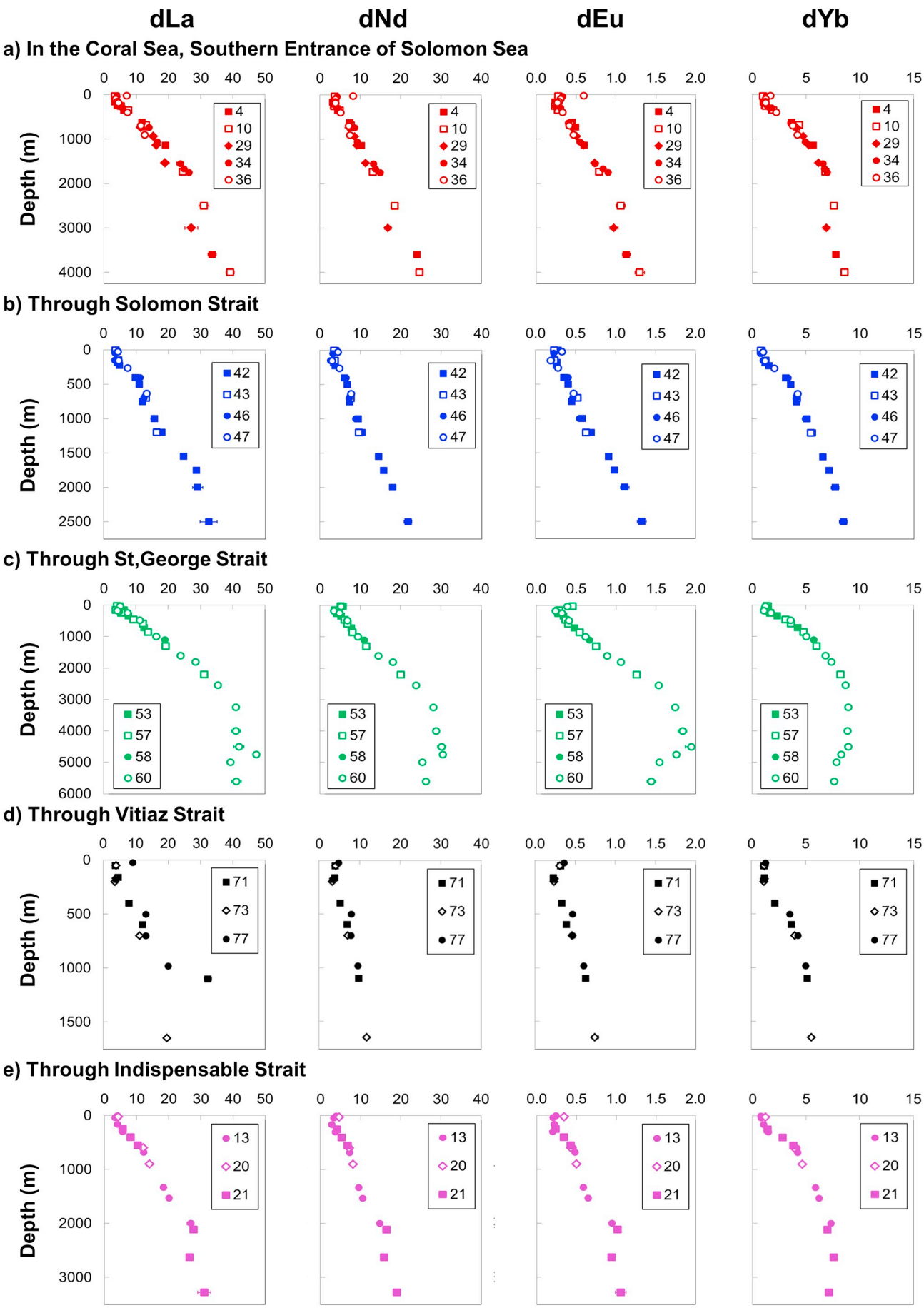

(caption on next page)

Fig. 3. Profiles of dissolved REE concentrations for La, Nd, Eu and Yb. Stations are gathered into five groups with the color codes consistent with their geographical location as proposed in Fig. 1.

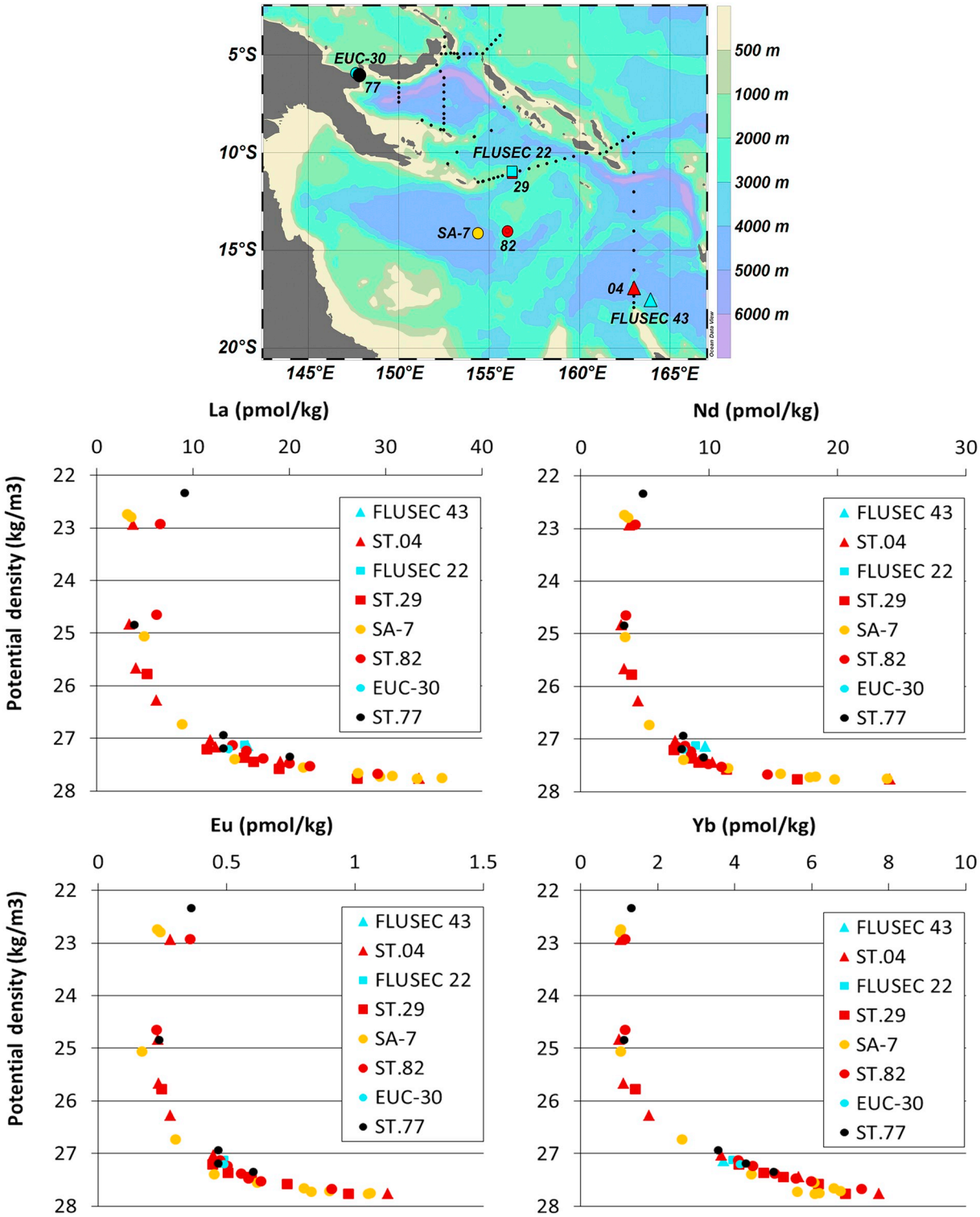

Fig. 4. Comparison of our data with those measured in the framework of preceding studies. Yellow point represent data from station SA-7 (sampled during September–October 1992) located in the middle of the Coral Sea and measured by Zhang and Nozaki (1996). Aqua square, triangle and dot represent data measured at the entrance of Solomon (FLUSEC 22), Coral sea (FLUSEC 43) and at exiting Vitiaz Strait (EUC-30), respectively, measured by Grenier et al. (2013). It is noted that all sample using in study of Grenier was sampled in August–September 2006. Sampling date of our samples are reported in Table 1. (For interpretation of the references to color in this figure legend, the reader is referred to the web version of this article.)

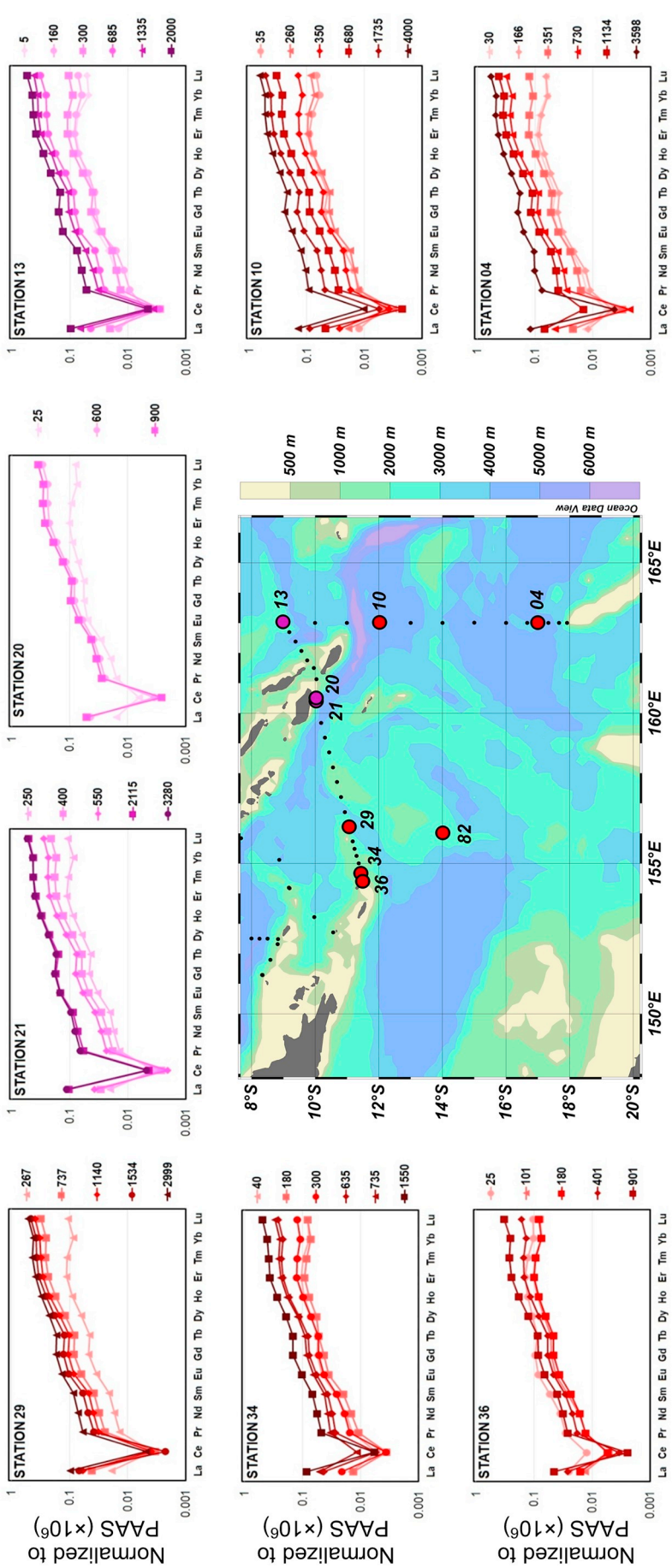

Fig. 5. dREE patterns normalized to PAAS ($\times 10^6$) at different depths for 8 stations sampled in the Coral Sea and at the entrance of Solomon Sea and for 12 stations located in the Solomon Sea and in the different straits. The light colors indicate shallow samples while darker colors represent the deeper ones.

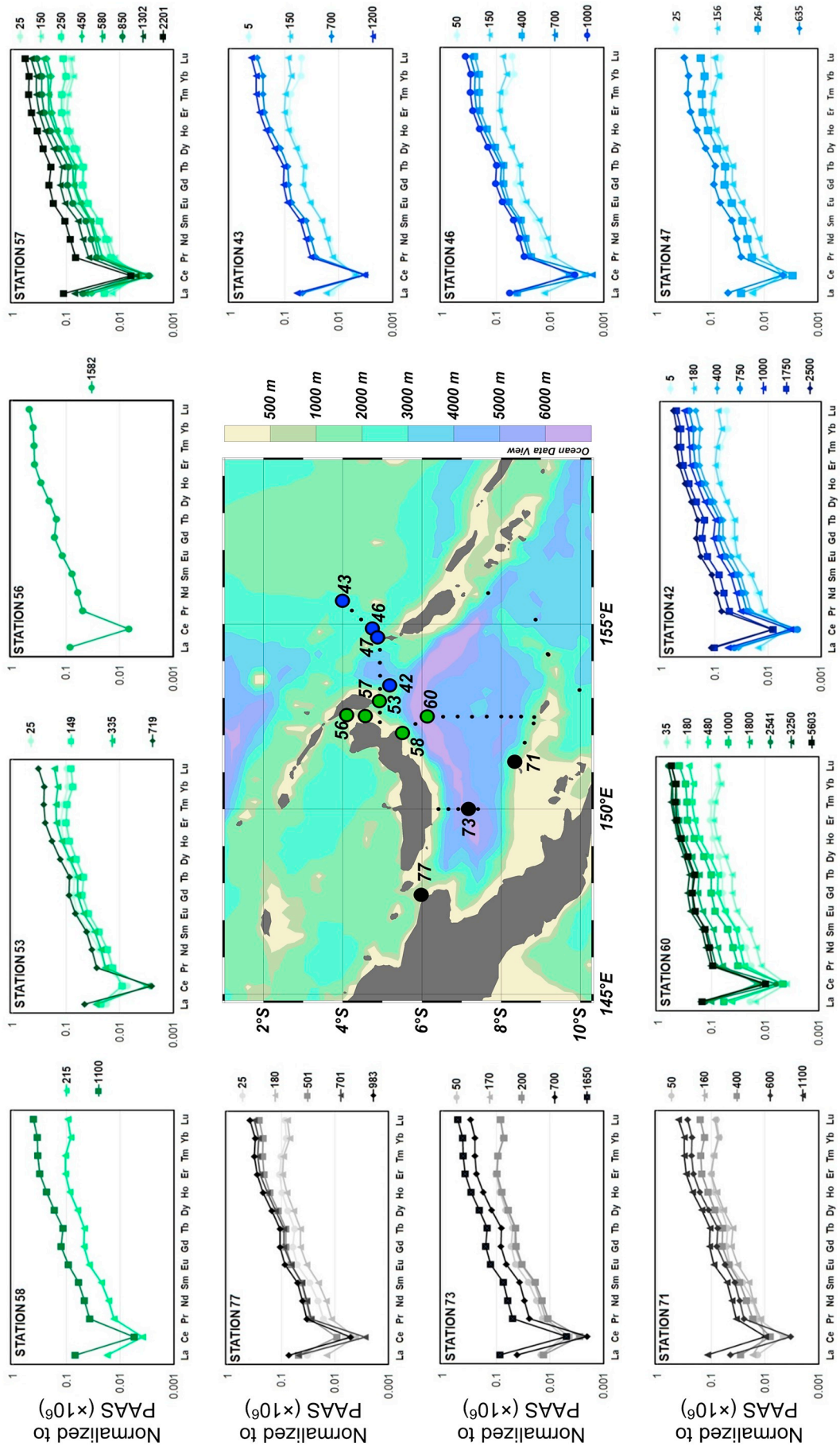

Fig. 5. (*continued*)

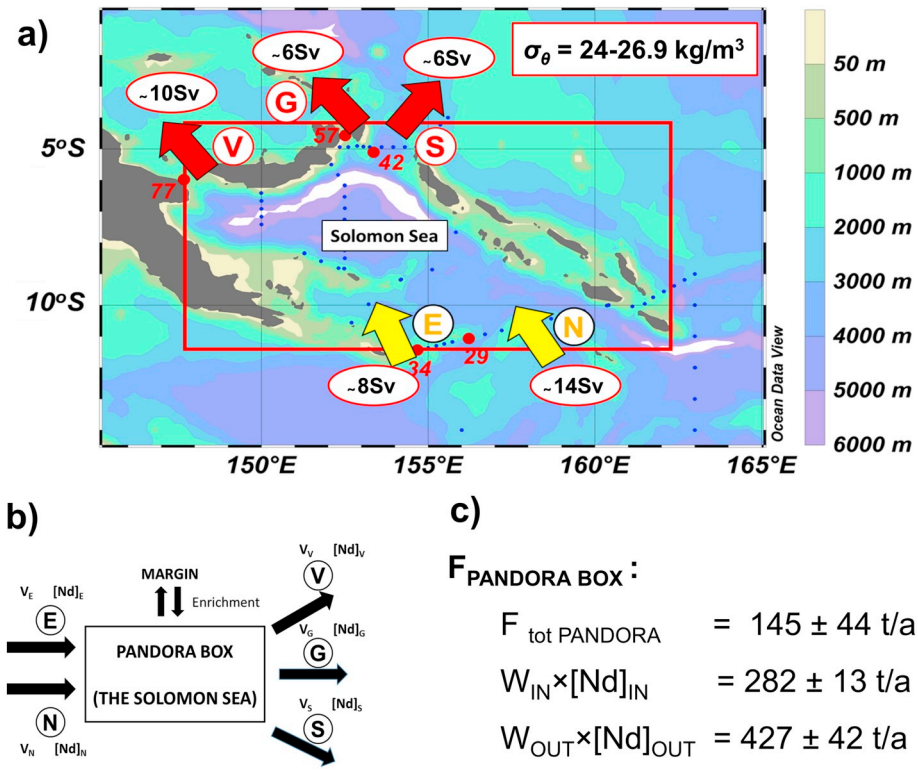

Fig. 6. a) Schematic description of the Pandora box (red rectangular). The water layer is defined in Table 4. Yellow arrows indicate southern input while red arrows characterize output flow through three straits. Meanwhile, colored letters coupled with number indicate different stations together with their transport. E: NGCU transport, N: direct NVJ transport, V, G and S: Vitiaz Strait, St George's Channel and Solomon Strait transports, respectively. b) Enrichment visualizing by simple Pandora box with 2 southern inputs and 3 northern outputs as presented in Fig. 6a. The Nd concentrations taken into account here are $[Nd]_E$, $[Nd]_N$ in the south and $[Nd]_S$, $[Nd]_G$ and $[Nd]_V$ in the north. c) Significant enrichment is observed at Lower Thermocline Water; all fluxes are reported in Table 4. (For interpretation of the references to color in this figure legend, the reader is referred to the web version of this article.)

Table 4
Water masses and associated volume transports (Sv) of different density layers during Pandora. The dNd fluxes were estimated from dNd values compiled in Table 3 and water transports entering and leaving the Solomon Sea.

Water mass	Upper σ_θ (kg/m^3)	Lower σ_θ (kg/m^3)	Incoming NGCU $\{W_E\}$	Direct NVJ $\{W_N\}$	Vitiaz $\{W_V\}$	St-Georges $\{W_G\}$	Solomon $\{W_S\}$	dNd flux (ton/year)
UTW	24	25.3	1.5 ± 0.5	3.5 ± 0.5	1.5 ± 0.5	1.5 ± 0.5	2.0 ± 0.5	1 ± 16
LTW	25.3	26.9	9.2 ± 0.5	7.8 ± 0.5	8.0 ± 0.5	4.0	5 ± 0.5	145 ± 45
IW	26.9	27.4	7.2 ± 1.0	1.2 ± 1.0	4.5	1.4	2.5 ± 1.0	-4 ± 51
UCDW - upper extent	27.4	27.65	1.0 ± 0.5	4.5 ± 1.5	–	1.5 ± 0.5	4.0 ± 0.5	49 ± 104
UCDW - lower extent	27.65	27.76	–	3.0 ± 2.0	–	0.5	2.5 ± 2.0	25 ± 138

PANDORA cruise data (Ganachaud et al., 2017; Germineaud et al., 2016). Currents were recorded along the ship track with Shipboard Acoustic Doppler Current Profilers (S-ADCPs) with a vertical extent of around 1000–1300 m. S-ADCPs were rotated to estimate the current perpendicular to each of the box model section (Germineaud et al., 2016). Deeper than 1000 m, they are combined with geostrophic velocities estimated with CTD station pairs, and referenced to 3000 m depth, or to the deepest common level of the station pairs.

Transports computed across the southern entrance do not balance the summed transports at the exits, as they were estimated during instantaneous transects. For the purpose of this study, relying on a steady state hypothesis, velocities are adjusted with an inverse model allowing the mass, salt and heat conservation (Germineaud et al., 2016). The water transports and associated uncertainties are given, for each layer, in Table 4.

The calculation is reported in Fig. 6c for Nd in the lower thermocline layer, and budgets for the other layers are reported in Table 4. The only missing dREE concentration data are for the upper thermocline at station 29. We therefore estimated these values using its neighbor stations due to their similarity in dREE concentrations (stations 04, 34 and 36). The sign of $F_{tot\ PANDORA}$ indicates whether external input of Nd (when positive) or subtraction by scavenging process (when negative) dominates along the pathways of the different water layers. A Monte Carlo statistic method (normal distribution, $n = 1000$) was used to estimate uncertainties of the fluxes.

A significant positive net flux ($F_{total\ PANDORA} = 145 \pm 46$ t(Nd)/year; Fig. 6c) is estimated in the lower thermocline, suggesting that waters leaving the Solomon Sea export more dNd than waters entering the Solomon Sea, indicating a net gain of dNd in this layer. Grenier et al. (2014) did not show any enrichment of this layer upstream the Solomon Sea while they similarly found a dNd enrichment downstream, more specifically along the Papua New Guinea coast. The present study fills a gap of this preceding work by showing that dNd enrichment also occurs within the Solomon Sea. Both studies demonstrate that the Lower Thermocline is enriched before filling the Equatorial Undercurrent. Enrichments are also observed in the other layers, except for IW. However, the large uncertainties affecting the calculated fluxes prevent us from drawing firm conclusions for these layers (Table 4).

Contrastingly, in the upper thermocline, our results do not show a clear and strong enrichment in Nd content. Our hypothesis is that the dNd (dREE) external inputs, likely weathered from the surrounding islands and discharged into the Solomon Sea, are balanced by the dNd (dREE) removal by scavenging, consistent with the productivity of the area (Radenac et al., 2013; Bonnet et al., 2016). This will be confirmed or disproved by the isotopic Nd measurements.

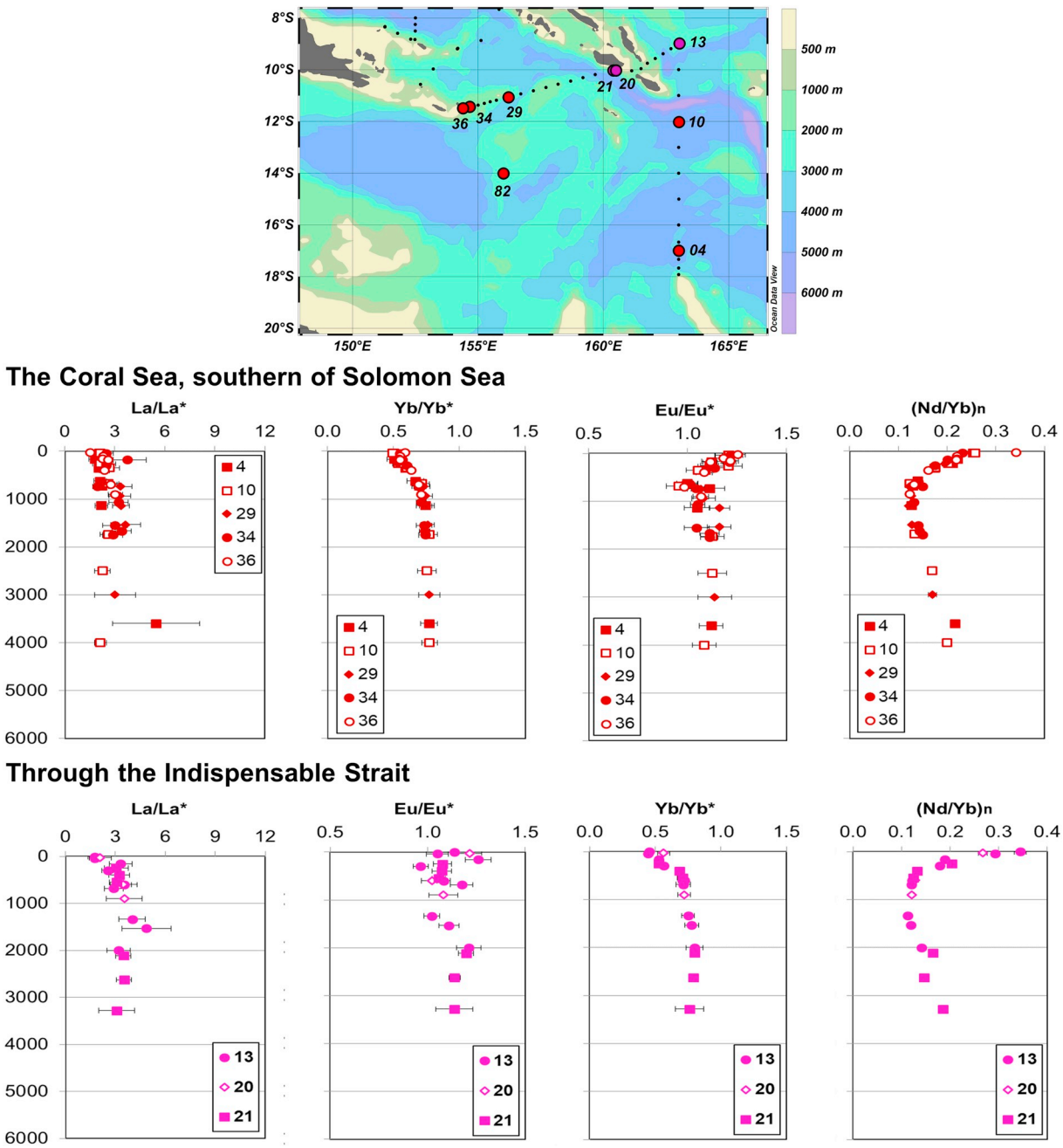

Fig. 7. Vertical profiles of the anomalies of La (La/La*), Eu (Eu/Eu*), Yb (Yb/Yb*) and of ratio $(Nd/Yb)_n$, calculated following Bau et al. (2004), Bau et al. (1996), Friend et al. (2008), and Garcia-Solsona et al. (2014). The color of markers follows the color code of Fig. 1. $(Nd/Yb)_n$ profiles are also reported after normalization to basalt (orange markers), for comparison with the PAAS-normalized ones.

5.2. Interesting features in the dREE profiles

This section discusses more specifically the dREE PAAS-normalized patterns and anomalies. Calculated dREE anomalies allow identifying if, after normalization to the PAAS values, an element is enriched or depleted relatively to its neighbors. Thus, they can bring information about the dominant mechanisms affecting the local marine REE pool. Anomalies are calculated following the equations below (Bau et al., 2004; Bau et al., 1996; Friend et al., 2008; Garcia-Solsona et al., 2014). In the following, we will discuss more specifically the La, Ce, Eu and Yb anomalies. The REE/REE* ratio reveals an enrichment relatively to its neighbors when its value is larger than one, and a depletion in the opposite case.

$$\frac{La}{La^*} = \frac{[La]_n}{3[Pr]_n - 2[Nd]_n} \quad (1)$$

$$\frac{Ce}{Ce^*} = \frac{[Ce]_n}{2[Pr]_n - [Nd]_n} \quad (2)$$

$$\frac{Eu}{Eu^*} = \frac{4 \times [Eu]_n}{3[Sm]_n + [Dy]_n} \quad (3)$$

$$\frac{Yb}{Yb^*} = \frac{[Yb]_n}{2[Er]_n + [Dy]_n} \quad (4)$$

A complementary parameter to the anomalies is the ratio between normalized LREEs and HREEs, expressed as Nd_n/Yb_n, which provides information about the slope of the normalized dREE pattern. Fig. 7 shows the vertical profiles for the La, Eu, Yb anomalies and the Nd_n/Yb_n

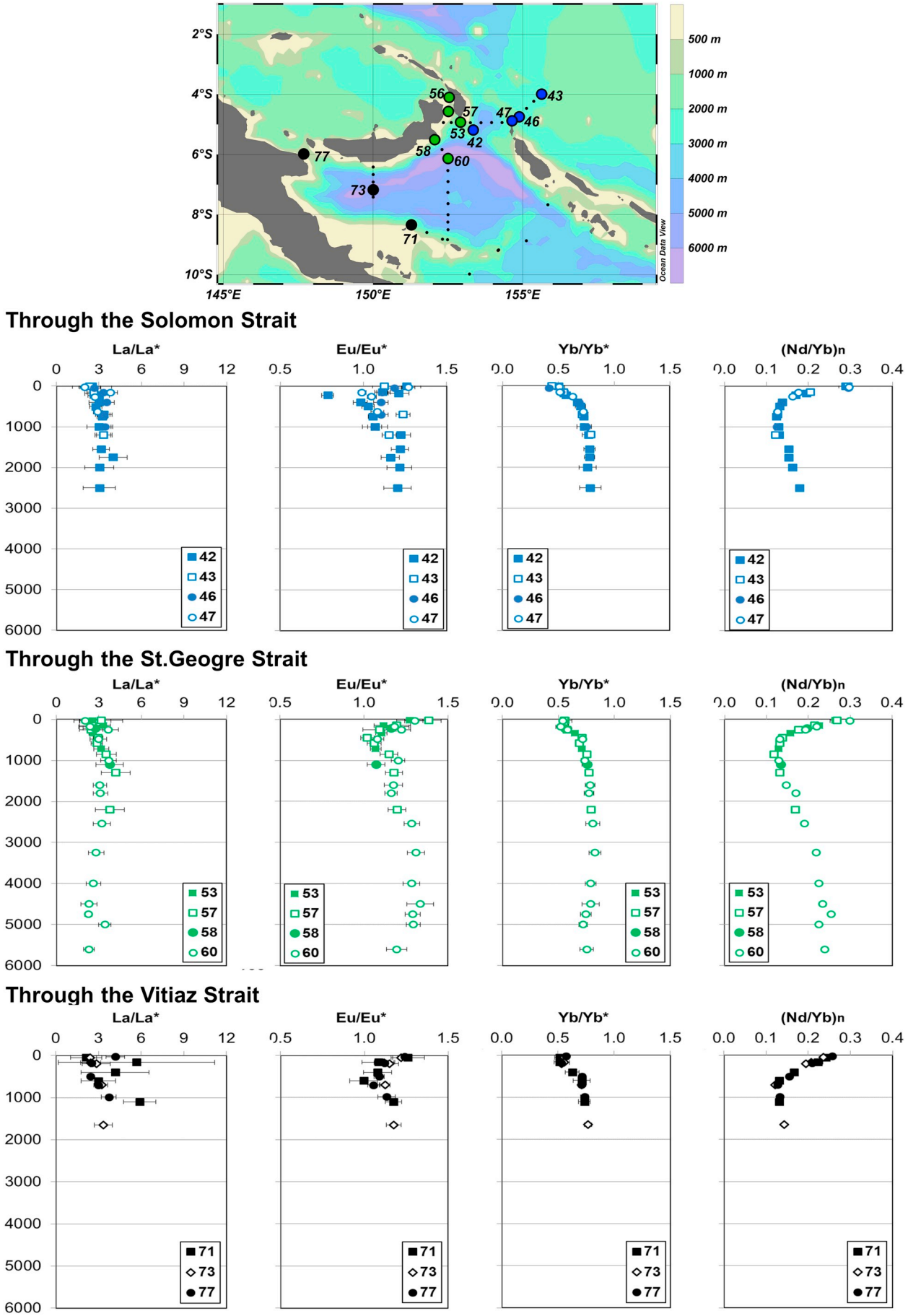

Fig. 7. (*continued*)

slope. Normalization of the dREEs to PAAS suggests that without any fractionation between the dREEs within the water column, the dREE pattern would be flat -Nd_n/Yb_n equal to 1- or marked by a slight positive Eu anomaly if the lithogenic material is basaltic (Grenier et al., 2013). The full data set is reported in Table 1.

5.2.1. Dissolved lanthanum anomaly

All the dissolved Solomon Sea samples collected during Pandora are characterized by positive La anomalies, with values ranging from 3 to 6 (Fig. 7). Such positive values have been observed elsewhere in the ocean (e.g. Garcia-Solsona et al., 2014; Grenier et al., 2018) and are believed to result from a differential La behavior due to the lacking electron in the 4f shell of the La atom, suspected to increase its stability in seawater, so called the "tetrad" or "double-double" effect (Byrne and Kim, 1990; Byrne and Sholkovitz, 1996; De Baar et al., 1985b; Elderfield et al., 1988; Garcia-Solsona et al., 2014; Grenier et al., 2018; Lee and Byrne, 1993; McLennan, 1994). In particular, while dLa is released from riverine particles when freshwaters are discharged into the ocean, more efficient releasing than scavenging rate could cause local positive dLa anomalies (Lawrence and Kamber, 2006).

Nevertheless, the positive dLa anomalies in the Solomon Sea are observed at all the monitored stations, even those located far from the coastline. The oceanic dREE pattern may results from dissolved-particle exchange also occurring in the open ocean (Byrne and Kim, 1990; Schijf et al., 2015; Tachikawa et al., 1999), so we are seeking if another factor than the "Tetrad effect" only could govern the La behavior in the Coral and Solomon Seas.

Due to the similar atomic size and close chemical properties of barium and lanthanum, they are suspected to display coupled behavior in seawater (Garcia-Solsona et al., 2014; Haley et al., 2014; Grenier et al., 2018). Bishop (1988) and Dehairs et al. (1980) demonstrated that oceanic dBa distribution is governed by the surface biologically driven formation of barite crystal ($BaSO_4$) followed by its dissolution at depth. Coupling between the two elements could therefore occur if dLa is associated to the dBa/barite cycle within the water column (Dehairs et al., 1980; Garcia-Solsona et al., 2014; Grenier et al., 2018; Guichard et al., 1979). Although significant correlations between dLa and dBa concentrations were observed at some stations in the Solomon Sea, these correlations do not hold when incorporated in a plot representing the world ocean dBa and dLa data, extracted from the GEOTRACES IDP 2017 (see Fig. A3 and A4, supplementary material). We therefore consider that our data do not help assessing the dLa-dBa link.

A third mechanism that could yield La fractionation is of microbial origin. Indeed, Shiller et al. (2017) revealed that some methanotroph bacteria require LREE and more specifically La as enzyme co-factor. However, it seems that this processus substracts La from the water column, while we observe a La enrichment. In any case, this hypothesis needs further investigation.

5.2.2. Dissolved europium anomaly

All normalized dREE patterns display a positive Eu anomaly whatever the water mass type and sample location. Such positive dEu anomalies were observed in previous studies (Amakawa et al., 2000; Nozaki et al., 1999) but were not discussed till the work of Zhang et al. (2008) and the more recent observations of Grenier et al. (2013, 2018). Either on the Kerguelen plateau (Grenier et al., 2018; Zhang et al., 2008) or in the Equatorial Pacific (Grenier et al., 2013) these authors invoke a remaining signature of lithogenic inputs of basaltic origin, local basalts being characterized by a positive Eu anomaly.

In our studied area, the dEu shows maxima in the surface water, reach a minimum at intermediate depths (~500 m) and then slightly increase again toward bottom except in the Coral Sea profiles characterized by fairly constant dEu anomalies at depths below 1000 m (Fig. 7).

The higher dEu anomalies (~1.3) at the surface likely reflect recent enrichments of lithogenic origin, which could be of coastal or atmospheric source. Indeed, the Solomon Sea is surrounded by volcanic islands whose basaltic material is enriched in Eu (Grenier et al., 2013). Basalt REE patterns (normalized to PAAS) originating from the New Britain (Holm et al., 2013) and (Kelemen et al., 2013). Tonga islands are reported in Fig. A5. While quite different in shape, both displays a marked positive Eu anomaly, confirming the Eu enrichment in these outcropping material. Besides, some volcanoes such as Rabaul, Ulawun and Bagana, are still very active (Lefèvre et al., 2008; Slemons et al., 2010). The variable REE basailt patterns shown in Fig. A5a makes difficult to select one of those to normalize our seawater dREE datato the local material. However, Fig. A5b displays the Eu anomaly profiles when normalized to the 3 basalt REE values. The resulting negative anomalies suggest that internal processes modified the relative abundance of Eu to its trivalent neighbors.

Deeper than 1000 m, the positive dEu anomaly increase could result from two non-exclusive processes. The first presumed process is the release of dREE in intermediate and deep layers caused by the dissolution of basaltic sediments deposited on the margins by submarine weathering followed by the advection of the enriched waters (Grenier et al., 2013; Jeandel et al., 2011; Zhang et al., 2008). As already underlined by Grenier et al. (2013), the preservation of this dEu anomaly is made possible by the fact that the residence time of dEu (320–820 years; Alibo and Nozaki, 1999) is larger than that of the thermocline waters across the studied area (10–15 years, Fukumori et al., 2004). Another explanation was recently suggested by Grenier et al. (2018): the deep positive dEu anomaly may also result from LREE/MREE preferential scavenging onto surface coating of organic particles in surface water followed by their release at depth (Sholkovitz et al., 1994). Ongoing measurements of the filtered particles might help to characterize the importance of such processes in the Solomon Sea.

5.2.3. Dissolved cerium anomalies

Contrastingly to dLa and dEu, the marked depletion of dCe is observed at almost all the studied stations, although less pronounced in the surface and subsurface waters above 500 m ($dCe/dCe^* \geq 0.4$). Consistent with the higher dEu anomalies discussed above, these less pronounced dCe anomalies might reflect recent lithogenic inputs, which likely impact preferentially the upper layers. Higher dCe anomalies ($dCe/dCe^* \geq 0.5$) were found mostly in the surface water of stations located around the Solomon archipelago (e.g. stations 42, 43, 60), indicating more recent inputs. Specifically, one sample in the upper thermocline at station 71 (160 m) shows a significantly high positive dCe anomaly (~1.4). However, this station is very close to the coast and was located here to identify any margin input to the waters conveyed by the NGCU through the split between Papua New Guinea main island and Woodlark island; the existence of strong inputs is thus confirmed by the high positive Ce anomaly observed at this station.

5.2.4. HREE behavior

The vertical dHREE profiles show more convex shapes than the other dREE ones (Fig. 3). In addition, the Nd_n/Yb_n slopes are increasing below intermediate depths at a rate of two up to the seafloor (Fig. 7). Such rapid increase was already observed although not always discussed (Grenier et al., 2018; Haley et al., 2014; Jeandel et al., 2013; Molina-Kescher et al., 2014). Bertram and Elderfield (1993) noticed that coupling between dREE and dSi cycle could be more significant for the dHREE than for the dLREE and recent field work of Akagi (2013) and Grenier et al. (2018) seem to confirm this observation. Here we propose to explore deeper the link between dHREE (represented by dYb) and the dSi cycle. In Fig. 8, only the data acquired in this work are reported. Fig. 8a shows that dNd relationship with dSi is dispersed, as shown by the correlation coefficients, ranging from 0.04 above the thermocline to 0.75 below. This contrasts with the better relationship observed between dYb and dSi in Fig. 8b ($R^2 = 0.66$ above the thermocline and 0.93 below). To go further, we extended this comparison to a broader scale (see Fig. A1 and A2 in the supplementary material).

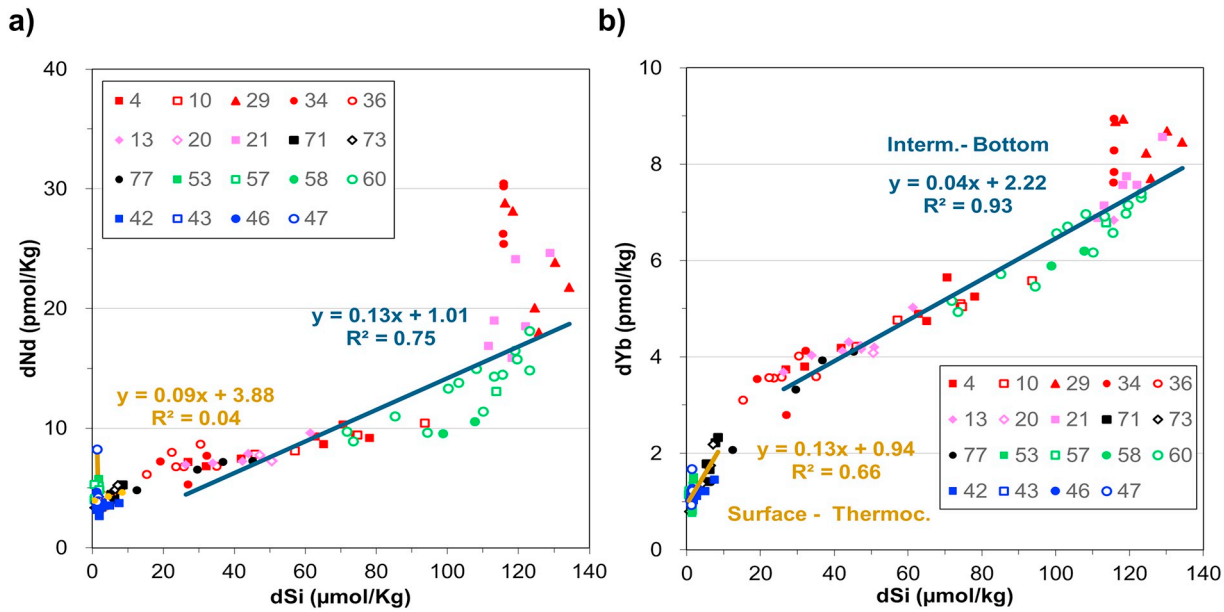

Fig. 8. Relationship between a) dNd and b) dYb (in pmol/kg) versus dSi (in µmol/kg) in Surface-Thermocline and Intermediate-Bottom layers in the Solomon Sea.

The comparison of the Solomon Sea data with the dREE data collected over the whole Atlantic Ocean shows the high values of the correlation coefficients (~R^2 = 0.9). This supports the hypothesis of a coupling between dYb and dSi except in the upper layers: for dSi concentrations below 20 µM, dSi and dYb data are more dispersed. The dLREE relationship with dSi is clearly different and more scattered than the dHREE one, as illustrated for dNd in Fig. A1. In the deep layers, the observed dYb/dSi slope of the linear fitting curve is consistent with the dEr/dSi one found by Bertram and Elderfield (1993) in the intermediate, deep and bottom waters of the Pacific Ocean (ΔdHREE/ΔdSi~0.04; see Fig. 8b of Bertram and Elderfield, 1993).

The shape of the global and local curves reflects several common features: for dSi < 20 µM, a faster release (rather than a slower removal; see below) of Yb than of Si generates a steep and very scattered slope; deeper, the increase rate of dYb significantly diminishes and is strongly correlated to the Si one. This could reflect differential release of Yb and Si from the particles, a fraction of Yb being adsorbed and easily released, and the remaining part being possibly absorbed in the silica tests as suggested by Akagi (2013). Another explanation could be that complexation between dREE and silicate (only found to be significant in the deep Pacific water; Patten and Byrne, 2017) could explain this differential behavior with depth between the 2 species. However, Patten and Byrne (2017) underline that we don't have so far the correct thermodynamic data for the whole series of REEs to conclude further. Similar break in the dYb/dSi slope was observed on the Kerguelen plateau (Grenier et al., 2018), but the lack of reliable kinetic and thermodynamic data invite to interpret cautiously the relationship between REE and the opal uptake/remineralization in the different oceanic environments.

Nevertheless, while there is no pronounced difference for the dYb-dSi ratio between the deep Atlantic and Pacific, Fig. 8b shows that for the same dSi content, dYb values are larger in the north Atlantic than in the south Atlantic or in the Pacific. Such gradient likely reflects the fact that the Si cycle is mostly driven by biological uptake-remineralization while Yb one is sensitive to lithogenic external inputs (more important in the Atlantic) and scavenged by different processes (adsorption, possible opal stripping…).

5.3. Origin of the dREE enrichments in the Solomon Sea

Based on features discussed in the preceding Subsection 5.2, the dNd (dREE) enrichment calculated with our box model (Section 5.1) likely results from the release of dNd (dREEs) from the surface and submarine weathering of the surrounding islands. Several complementary parameters allowed us to confirm the nature of this external dNd source and its signature in the dissolved phase. In this aim, the full set of measured dMn and dAl analyzed by Susanna Michael are proposed in Table C in the Supplementary material (Michael et al., submitted). Surface dEu enrichments and larger dCe values are consistent with similar high concentrations observed in the dAl and dMn profiles (Michael et al., submitted). In addition, consistent maxima of dREEs, dAl and dMn are also observed at some specific points in the thermocline and intermediate layers (i.e. stations 04-1000 m; 10-350 m; 20-700 m; 42–700 m; 71–300 m; 77–500 m). Such consistencies underline that submarine weathering took place along the island margins. The Solomon Sea is an area of strong internal wave activity and associated mixing (Alberty et al., 2017). It has been suggested that when the continental slope is close to a critical angle, the strong bottom shear velocities enhance sediment resuspension and potential release of chemical elements (Cacchione et al., 2002). Nepheloid layers might result from these processes and be advected further from the slope, contributing to the observed enrichments. The exact location of such resuspension events could be an interesting investigation for future studies.

6. Conclusion

This study presented vertical profiles of dREE concentrations for 143 samples and 21 stations collected in the Coral and Solomon Seas as part of the PANDORA cruise (summer 2012). Although the profile shapes display common dREE features -i.e. surface depleted and enriched at depth- the dREE patterns and anomalies could be discussed and lead to interesting results.

A pronounced dissolved positive dLa anomaly is estimated (dLa*/dLa varying between 3 and 6). Despite the interesting correlation between dBa and dLa in our data, we could not demonstrate that this anomaly was linked to the Ba-Barite cycle. This specific lanthanum behavior likely relates more to the “tetrad” effect. The future analysis of particulate La and biogenic particulate Ba may bring further information.

A ubiquitous europium positive anomaly is also found in the dREE patterns, with higher dEu/dEu* values in the upper layers. This striking

feature agrees with previous observations (Grenier et al., 2013, 2018; Zhang et al., 2008) and suggests that the enrichment calculated with the box model is of basaltic origin, consistent with the geology of the surrounding islands. The lithogenic character of this source is later supported by dCe anomaly.

dHREE behaviour seem to be mostly influenced by the Si cycle as suggested by Akagi (2013) and also observed by Grenier et al. (2018). However, HREE are also scavenged by adsorption on the settling particles, which explains differential fates of both tracers in the upper layers (dSi < 20 μM).

A box model allowed us to establish the net dNd (dREE) fluxes of the waters flowing equatorward through the Solomon Sea. Significant enrichment is observed for the Lower Thermocline Layer (between 200 and 500 m; F_{total} PANDORA = 145 ± 46 tons of Nd per year). This enrichment is of main interest, as these waters will eventually be advected till the equatorial eastern Pacific through the lower part of the EUC (Slemons et al., 2010; Grenier et al., 2011). By contrast, the lack of clear net enrichment in the upper thermocline is surprising in this area bounded by continental margins and with many potential sources. However, the large error bars prevent us from drawing conclusions about what is happening in other layers. This points to the complexity of boundary exchange processes and to the need of better understanding the removal processes of the oceanic dissolved material. The ongoing analysis of the associated particles and Nd isotopic composition will also help to refine our understanding of these net exchange fluxes.

Acknowledgements

This work is a contribution to the CLIVAR/SPICE and GEOTRACES International programs. We thank the technical division of INSU (DT-INSU) Olivier Desprez de Gesincourt and Lionel Fichen who made possible the various in situ measurements, thereby requiring skills and care. The collaboration with SOPAC/SPC, PI-GOOS, and University of Papua New Guinea was greatly appreciated. We also acknowledge Benjamin Dupont for his volunteering help during the on-board sampling. The accomplishments were made possible through concurrent contributions of national funding agencies. The Pandora cruise has been co-funded by NSF grant OCE1029487, and by ANR project ANR- 09-BLAN-0233-01 and INSU/LEFE project Solwara (IDAO and CYBER). All the authors whose work contributed to the database GEOTRACES are acknowledged (http://www.geotraces.org; http://www.solomonseaoceanography.org). Besides of that, we would like to thank the research TIM at LEGOS for insightful comment and encouragement. C. Pradoux and F. Candaudap are thanked for their technical supports.

Appendix A. Supplementary data

Supplementary data to this article can be found online at https://doi.org/10.1016/j.chemgeo.2019.05.012.

References

Abbott, A.N., Haley, B.A., McManus, J., Reimers, C.E., 2015. The sedimentary flux of dissolved rare earth elements to the ocean. Geochim. Cosmochim. Acta. https://doi.org/10.1016/j.gca.2015.01.010.

Akagi, T., 2013. Rare earth element (REE)-silicic acid complexes in seawater to explain the incorporation of REEs in opal and the 'leftover' REEs in surface water: new interpretation of dissolved REE distribution profiles. Geochim. Cosmochim. Acta. https://doi.org/10.1016/j.gca.2013.03.014.

Akagi, T., Fu, F., Hongo, Y., Takahashi, K., 2011. Composition of rare earth elements in settling particles collected in the highly productive North Pacific Ocean and Bering Sea: Implications for siliceous-matter dissolution kinetics and formation of two REE-enriched phases. Geochim. Cosmochim. Acta. https://doi.org/10.1016/j.gca.2011.06.001.

Alberty, M.S., Sprintall, J., et al., 2017. Spatial patterns of mixing in the Solomon Sea. Journal of Geophysical Research: Oceans 122, 4021–4039. https://doi.org/10.1002/2016JC012666.

Alibo, D.S., Nozaki, Y., 1999. Rare earth elements in seawater: particle association, shale-normalization, and Ce oxidation. Geochim. Cosmochim. Acta. https://doi.org/10.1016/S0016-7037(98)00279-8.

Amakawa, H., Alibo, D.S., Nozaki, Y., 2000. Nd isotopic composition and REE pattern in the surface waters of the eastern Indian Ocean and its adjacent seas. Geochim. Cosmochim. Acta 64, 1715–1727. https://doi.org/10.1016/S0016-7037(00)00333-1.

Bau, M., Koschinsky, A., Dulski, P., Heinz, J.R., 1996. Comparison of the Partitioning Behaviours of Yttrium, Rare Earth Elements, and Titanium between Hydrogenetic Marine Ferromanganese Crusts and Seawater.

Bau, M., Alexander, B., Chesley, J.T., Dulski, P., Brantley, S.L., 2004. Mineral dissolution in the Cape Cod aquifer, Massachusetts, USA: I. Reaction stoichiometry and impact of accessory feldspar and glauconite on strontium isotopes, solute concentrations, and REY distribution. Geochim. Cosmochim. Acta. https://doi.org/10.1016/j.gca.2003.08.015.

Behrens, M.K., Muratli, J., et al., 2016. Rapid and precise analysis of rare earth elements in small volumes of seawater - Method and intercomparison. Mar. Chem. https://doi.org/10.1016/j.marchem.2016.08.006.

Bertram, C.J., Elderfield, H., 1993. The geochemical balance of the rare earth elements and neodymium isotopes in the oceans. Geochim. Cosmochim. Acta. https://doi.org/10.1016/0016-7037(93)90087-D.

Bishop, J.K.B., 1988. The barite-opal-organic carbon association in oceanic particulate matter. Nature 332, 341–343. https://doi.org/10.1038/332341a0.

Bonnet, S., Berthelot, H., et al., 2016. Diazotroph derived nitrogen supports diatom growth in the South West Pacific: a quantitative study using nanoSIMS. Limnol. Oceanogr. https://doi.org/10.1002/lno.10300.

Bostock, H.C., Opdyke, B.N., Williams, M.J.M., 2010. Characterising the intermediate depth waters of the Pacific Ocean using δ13C and other geochemical tracers. Deep-Sea Research Part I: Oceanographic Research Papers. https://doi.org/10.1016/j.dsr.2010.04.005.

Byrne, R., Sholkovitz, E., 1996. Chapter 158 Marine Chemistry and Geochemistry of the Lanthanides. pp. 497–593. doi: https://doi.org/10.1016/S0168-1273(96)23009-0 (.).

Byrne, R.H., Kim, K.H., 1990. Rare earth element scavenging in seawater. Geochim. Cosmochim. Acta. https://doi.org/10.1016/0016-7037(90)90002-3.

Cacchione, D.A., Pratson, L.F., Ogston, A.S., 2002. The shaping of continental slopes by internal tides. Science. https://doi.org/10.1126/science.1069803.

Chung, C.H., Brenner, I., You, C.F., 2009. Comparison of microconcentric and membrane-desolvation sample introduction systems for determination of low rare earth element concentrations in surface and subsurface waters using sector field inductively coupled plasma mass spectrometry. Spectrochimica Acta - Part B Atomic Spectroscopy 64, 849–856. https://doi.org/10.1016/j.sab.2009.06.013.

Cravatte, S., Ganachaud, A., Duong, Q.P., Kessler, W.S., Eldin, G., Dutrieux, P., 2011. Observed circulation in the Solomon Sea from SADCP data. Prog. Oceanogr. https://doi.org/10.1016/j.pocean.2010.12.015.

Crusius, J., Calvert, S., Pedersen, T., Sage, D., 1996. Rhenium and molybdenum enrichments in sediments as indicators of oxic, suboxic and sulfidic conditions of deposition. Earth Planet. Sci. Lett. https://doi.org/10.1016/S0012-821X(96)00204-X.

Davis, R.E., Kessler, W.S., Sherman, J.T., Davis, R.E., Kessler, W.S., Sherman, J.T., 2012. Gliders measure western boundary current transport from the South Pacific to the equator*. J. Phys. Oceanogr. 42, 2001–2013. https://doi.org/10.1175/JPO-D-12-022.1.

De Baar, H.J.W., Bacon, M.P., Brewer, P.G., 1983. Rare-earth distributions with a positive Ce anomaly in the Western North Atlantic Ocean. Nature 301, 324–327. https://doi.org/10.1038/301324a0.

De Baar, H.J.W., Brewer, P.G., Bacon, M.P., 1985a. Anomalies in rare earth distributions in seawater: Gd and Tb. Geochim. Cosmochim. Acta. https://doi.org/10.1016/0016-7037(85)90090-0.

De Baar, H.J.W., Bacon, M.P., Brewer, P.G., Bruland, K.W., 1985b. Rare earth elements in the Pacific and Atlantic Oceans. Geochim. Cosmochim. Acta. https://doi.org/10.1016/0016-7037(85)90089-4.

Dehairs, F., Chesselet, R., Jedwab, J., 1980. Discrete suspended particles of barite and the barium cycle in the open ocean. Earth Planet. Sci. Lett. 49, 528–550. https://doi.org/10.1016/0012-821X(80)90094-1.

Elderfield, H., 1990. Tracers of ocean paleoproductivity and paleochemistry: an introduction. Paleoceanography 5, 711–717. https://doi.org/10.1029/PA005i005p00711.

Elderfield, H., Sholkovitz, E.R., 1987. Rare earth elements in the pore waters of reducing nearshore sediments. Earth Planet. Sci. Lett. https://doi.org/10.1016/0012-821X(87)90202-0.

Elderfield, H., Whitfield, M., Burton, J.D., Bacon, M.P., Liss, P.S., 1988. The oceanic chemistry of the rare-earth elements [and discussion]. Philos. Trans. R. Soc. A Math. Phys. Eng. Sci. 325, 105–126. https://doi.org/10.1098/rsta.1988.0046.

Elrod, V.A., Berelson, W.M., Coale, K.H., Johnson, K.S., 2004. The flux of iron from continental shelf sediments: a missing source for global budgets. Geophys. Res. Lett. https://doi.org/10.1029/2004GL020216.

Fine, R.A., Lukas, R., Bingham, F.M., Warner, M.J., Gammon, R.H., 1994. The western equatorial Pacific: a water mass crossroads. J. Geophys. Res. https://doi.org/10.1029/94JC02277.

van de Flierdt, T., Pahnke, K., et al., 2012. GEOTRACES intercalibration of neodymium isotopes and rare earth element concentrations in seawater and suspended particles. Part 1: Reproducibility of results for the international intercomparison. Limnol. Oceanogr. Methods. https://doi.org/10.4319/lom.2012.10.234.

Freydier, R., Dupre, B., Polve, M., 1995. Analyses by inductively coupled plasma mass spectrometry of Ba concentrations in water and rock samples. Comparison between isotope dilution and external calibration with or without internal standard. European Journal of Mass Spectrometry 1, 283. https://doi.org/10.1255/ejms.140.

Friend, C.R.L., Nutman, A.P., Bennett, V.C., Norman, M.D., 2008. Seawater-like trace element signatures (REE + Y) of Eoarchaean chemical sedimentary rocks from southern West Greenland, and their corruption during high-grade metamorphism. Contrib. Mineral. Petrol. https://doi.org/10.1007/s00410-007-0239-z.

Fukumori, I., Lee, T., Cheng, B., Menemenlis, D., 2004. The Origin, Pathway, and Destination of Niño-3 Water estimated by a simulated Passive Tracer and its Adjoint. J. Phys. Oceanogr. https://doi.org/10.1175/2515.1.

Ganachaud, A., Cravatte, S., et al., 2014. The Southwest Pacific Ocean circulation and climate experiment (SPICE). Journal of Geophysical Research: Oceans. https://doi.org/10.1002/2013JC009678.

Ganachaud, A., Cravatte, S., et al., 2017. The Solomon Sea: its circulation, chemistry, geochemistry and biology explored during two oceanographic cruises. Elem Sci Anth. https://doi.org/10.1525/elementa.221.

Garcia-Solsona, E., Jeandel, C., Labatut, M., Lacan, F., Vance, D., Chavagnac, V., Pradoux, C., 2014. Rare earth elements and Nd isotopes tracing water mass mixing and particle-seawater interactions in the SE Atlantic. Geochim. Cosmochim. Acta. https://doi.org/10.1016/j.gca.2013.10.009.

Gasparin, F., Ganachaud, A., Maes, C., 2011. A western boundary current east of New Caledonia: Observed characteristics. Deep-Sea Research Part I: Oceanographic Research Papers. https://doi.org/10.1016/j.dsr.2011.05.007.

Gasparin, F., Maes, C., Sudre, J., Garcon, V., Ganachaud, A., 2014. Water mass analysis of the Coral Sea through an Optimum Multiparameter method. Journal of Geophysical Research: Oceans 119, 7229–7244. https://doi.org/10.1002/2014JC010246.

German, C.R., Elderfield, H., 1989. Rare earth elements in Saanich Inlet, British Columbia, a seasonally anoxic basin. Geochim. Cosmochim. Acta. https://doi.org/10.1016/0016-7037(89)90128-2.

Germineaud, C., 2016. Circulation Océanique et Variabilité en Mer Des Salomon. Université Toulouse 3 Paul Sabatier (UT3 Paul Sabatier) (240 pp).

Germineaud, C., Ganachaud, A., et al., 2016. Pathways and water mass properties of the thermocline and intermediate waters in the Solomon Sea. J. Phys. Oceanogr. 46, 3031–3049. https://doi.org/10.1175/JPO-D-16-0107.1.

Goldberg, E.D., Koide, M., Schmitt, R.A., Smith, R.H., 1963. Rare-Earth distributions in the marine environment. J. Geophys. Res. https://doi.org/10.1029/JZ068i014p04209.

Goldstein, S.L., Hemming, S.R., 2003. Long-lived Isotopic Tracers in Oceanography, Paleoceanography, and Ice-sheet Dynamics. In: Treatise on Geochemistry. Elsevier, pp. 453–489. https://doi.org/10.1016/B0-08-043751-6/06179-X.

Grenier, M., Cravatte, S., et al., 2011. From the western boundary currents to the Pacific equatorial undercurrent: modeled pathways and water mass evolutions. Journal of Geophysical Research: Oceans. https://doi.org/10.1029/2011JC007477.

Grenier, M., Jeandel, C., Lacan, F., Vance, D., Venchiarutti, C., Cros, A., Cravatte, S., 2013. From the subtropics to the central equatorial Pacific Ocean: Neodymium isotopic composition and rare earth element concentration variations. Journal of Geophysical Research: Oceans. https://doi.org/10.1029/2012JC008239.

Grenier, M., Jeandel, C., Cravatte, S., 2014. From the subtropics to the equator in the Southwest Pacific: Continental material fluxes quantified using neodymium data along modeled thermocline water pathways. Journal of Geophysical Research: Oceans. https://doi.org/10.1002/2013JC009670.

Grenier, M., Garcia-Solsona, E., et al., 2018. Differentiating lithogenic supplies, water mass transport, and biological processes on and off the Kerguelen Plateau using rare earth element concentrations and neodymium isotopic compositions. Front. Mar. Sci. https://doi.org/10.3389/fmars.2018.00426.

Guichard, F., Church, T.M., Treuil, M., Jaffrezic, H., 1979. Rare earths in barites: distribution and effects on aqueous partitioning. Geochim. Cosmochim. Acta. https://doi.org/10.1016/0016-7037(79)90088-7.

Haley, B.A., Klinkhammer, G.P., McManus, J., 2004. Rare earth elements in pore waters of marine sediments. Geochim. Cosmochim. Acta. https://doi.org/10.1016/j.gca.2003.09.012.

Haley, B.A., Frank, M., Hathorne, E., Pisias, N., 2014. Biogeochemical implications from dissolved rare earth element and Nd isotope distributions in the Gulf of Alaska. Geochim. Cosmochim. Acta. https://doi.org/10.1016/j.gca.2013.11.012.

Hanawa, K., Talley, L.D., 2001. Eds. In: Siedler, G., Church, J., Gould, W.J. (Eds.), Mode Waters. Ocean Circulation and Climate: Observing and Modelling the Global Ocean. Academic, San Diego, Calif. London, pp. 373–386.

Holm, R.J., Spandler, C., Richards, S.W., 2013. Melanesian arc far-field response to collision of the Ontong Java Plateau: Geochronology and petrogenesis of the Simuku Igneous complex, New Britain, Papua New Guinea. Tectonophysics 603, 189–212. https://doi.org/10.1016/j.tecto.2013.05.029.

Jacquet, S.H.M., Dehairs, F., Cardinal, D., Navez, J., Delille, B., 2005. Barium distribution across the Southern Ocean frontal system in the Crozet–Kerguelen Basin. Mar. Chem. 95, 149–162. https://doi.org/10.1016/j.marchem.2004.09.002.

Jeandel, C., et al., 2011. Ocean margins: the missing term in oceanic element budgets? Eos, Transactions American Geophysical Union 92 (26), 217–218.

Jeandel, C., Delattre, H., Grenier, M., Pradoux, C., Lacan, F., 2013. Rare earth element concentrations and Nd isotopes in the Southeast Pacific Ocean. Geochem. Geophys. Geosyst. https://doi.org/10.1029/2012GC004309.

Johannesson, K.H., Chevis, D.A., Burdige, D.J., Cable, J.E., Martin, J.B., Roy, M., 2011. Submarine groundwater discharge is an important net source of light and middle REEs to coastal waters of the Indian River Lagoon, Florida, USA. Geochim. Cosmochim. Acta. https://doi.org/10.1016/j.gca.2010.11.005.

Johnson, G.C., Toolet, J.M., 1993. Flow of Deep and Bottom Waters in the Pacific at 10°N.

Johnson, K.S., Elrod, V.A., et al., 2003. Surface ocean-lower atmosphere interactions in the northeast Pacific ocean gyre: aerosols, iron, and the ecosystem response. Glob. Biogeochem. Cycles. https://doi.org/10.1029/2002GB002004.

Kawabe, M., Fujio, S., 2010. Pacific ocean circulation based on observation. J. Oceanogr. 66, 389–403. https://doi.org/10.1007/s10872-010-0034-8.

Kelemen, P.B., Hanghøj, K., Greene, A.R., 2013. One view of the geochemistry of subduction-related magmatic arcs, with an emphasis on primitive andesite and lower crust. In: Treatise on Geochemistry, Second edition. Elsevier, Oxford, pp. 749–806. https://doi.org/10.1016/B978-0-08-095975-7.00323-5.

Keppler, L., Cravatte, S., Chaigneau, A., Pegliasco, C., Gourdeau, L., Singh, A., 2018. Observed characteristics and vertical structure of Mesoscale Eddies in the southwest tropical Pacific. Journal of Geophysical Research: Oceans 123, 2731–2756. https://doi.org/10.1002/2017JC013712.

Kessler, W.S., 1999. Interannual variability of the subsurface high salinity tongue south of the equator at 165°E*. J. Phys. Oceanogr. 29, 2038–2049. https://doi.org/10.1175/1520-0485(1999)029<2038:IVOTSH>2.0.CO;2.

Kessler, W.S., Cravatte, S., 2013. Mean circulation of the Coral sea. Journal of Geophysical Research: Oceans. https://doi.org/10.1002/2013JC009117.

Klinkhammer, G.P., Chan, L.H., 1990. Determination of barium in marine waters by isotope dilution inductively coupled plasma mass spectrometry. Anal. Chim. Acta 232, 323–329. https://doi.org/10.1016/S0003-2670(00)81249-0.

Lacan, F., Jeandel, C., 2001. Tracing Papua New Guinea imprint on the central equatorial Pacific Ocean using neodymium isotopic compositions and rare earth element patterns. Earth Planet. Sci. Lett. https://doi.org/10.1016/S0012-821X(01)00263-1.

Lawrence, M.G., Kamber, B.S., 2006. The behaviour of the rare earth elements during estuarine mixing-revisited. Mar. Chem. https://doi.org/10.1016/j.marchem.2005.11.007.

Lee, Jong Hyeon, Byrne, R.H., 1993. Complexation of trivalent rare earth elements (Ce, Eu, Gd, Tb, Yb) by carbonate ions. Geochim. Cosmochim. Acta. https://doi.org/10.1016/0016-7037(93)90432-V.

Lefèvre, D., Guigue, C., Obernosterer, I., 2008. The metabolic balance at two contrasting sites in the Southern Ocean: The iron-fertilized Kerguelen area and HNLC waters. In: Deep-Sea Research Part II: Topical Studies in Oceanography, https://doi.org/10.1016/j.dsr2.2007.12.006.

Liu, Y.G., Miah, M.R.U., Schmitt, R.A., 1988. Cerium: a chemical tracer for paleo-oceanic redox conditions. Geochim. Cosmochim. Acta. https://doi.org/10.1016/0016-7037(88)90207-4.

Mackey, D.J., O'Sullivan, J.E.Os., Watson, R.J., 2002. Iron in the western Pacific: a riverine or hydrothermal source for iron in the Equatorial Undercurrent? Deep-Sea Res. I Oceanogr. Res. Pap. 49, 877–893. https://doi.org/10.1016/S0967-0637(01)00075-9.

McCartney, M.S., 1977. Subantartic Mode Water, Geogre Deacon 70th Anniversary. Voyage of Discovery, vol. Volume A. pp. 103–119.

McLennan, M., 1989. Rare earth elements in sedimentary rocks; influence of provenance and sedimentary processes. Rev. Mineral. Geochem. 21 (1), 169–200.

McLennan, M., 1994. Rare earth element geochemistry and the tetrad effect. Geochim. Cosmochim. Acta 58, 2025–2033.

Michael, S., et al., 2019. Constraining the Solomon Sea as a Source of Al and Mn to the Equatorial Undercurrent. (Submitted in 2019).

Milliman, J.D., Farnsworth, K.L., Albertin, C.S., 1999. Flux and fate of fluvial sediments leaving large islands in the East Indies. J. Sea Res. 41, 97–107. https://doi.org/10.1016/S1385-1101(98)00040-9.

Molina-Kescher, M., Frank, M., Hathorne, E., 2014. South Pacific dissolved Nd isotope compositions and rare earth element distributions: water mass mixing versus biogeochemical cycling. Geochim. Cosmochim. Acta. https://doi.org/10.1016/j.gca.2013.11.038.

Nozaki, Y., 1986. 226Ra222Rn210Pb systematics in seawater near the bottom of the ocean. Earth Planet. Sci. Lett. https://doi.org/10.1016/0012-821X(86)90017-8.

Nozaki, Y., Alibo, D.S., 2003a. Dissolved rare earth elements in the Southern Ocean, southwest of Australia: unique patterns compared to the South Atlantic data. Geochem. J. https://doi.org/10.2343/geochemj.37.47.

Nozaki, Y., Alibo, D.S., 2003b. Importance of vertical geochemical processes in controlling the oceanic profiles of dissolved rare earth elements in the northeastern Indian Ocean. Earth Planet. Sci. Lett. https://doi.org/10.1016/S0012-821X(02)01027-0.

Nozaki, Y., Alibo, D.S., Amakawa, H., Gamo, T., Hasumoto, H., 1999. Dissolved rare earth elements and hydrography in the Sulu Sea. Geochim. Cosmochim. Acta. https://doi.org/10.1016/S0016-7037(99)00142-8.

Orsi, A.H., Johnson, G.C., Bullister, J.L., 1999. Circulation, mixing, and production of Antarctic Bottom Water. Prog. Oceanogr. 43, 55–109. https://doi.org/10.1016/S0079-6611(99)00004-X.

Pahnke, K., van de Flierdt, T., Jones, K.M., Lambelet, M., Hemming, S.R., Goldstein, S.L., 2012. GEOTRACES intercalibration of neodymium isotopes and rare earth element concentrations in seawater and suspended particles. Part 2: Systematic tests and baseline profiles. Limnol. Oceanogr. Methods. https://doi.org/10.4319/lom.2012.10.252.

Patten, J.T., Byrne, R.H., 2017. Assessment of Fe(III) and Eu(III) complexation by silicate in aqueous solutions. Geochim. Cosmochim. Acta 202, 361–373. https://doi.org/10.1016/j.gca.2016.12.004.

Piepgras, D.J., Jacobsen, S.B., 1992. The behavior of rare earth elements in seawater: Precise determination of variations in the North Pacific water column. Geochim. Cosmochim. Acta. https://doi.org/10.1016/0016-7037(92)90315-A.

Qin, X., Menviel, L., Sen Gupta, A., van Sebille, E., 2016. Iron sources and pathways into the Pacific Equatorial Undercurrent. Geophys. Res. Lett. https://doi.org/10.1002/2016GL070501.

Qu, T., Lindstrom, E.J., 2002. A climatological interpretation of the circulation in the Western South Pacific*. J. Phys. Oceanogr. https://doi.org/10.1055/s-2007-989442.

Qu, T., Lindstrom, E.J., 2004. Northward intrusion of antarctic intermediate water in the Western Pacific*. J. Phys. Oceanogr. 34, 2104–2118. https://doi.org/10.1175/1520-0485(2004)034<2104:NIOAIW>2.0.CO;2.

Qu, T., Gao, S., Fukumori, I., Fine, R.A., Lindstrom, E.J., 2008. Subduction of South Pacific waters. Geophys. Res. Lett. https://doi.org/10.1029/2007GL032605.

Qu, T., Gao, S., Fukumori, I., Fine, R.A., Lindstrom, E.J., 2009. Origin and pathway of

equatorial 13°C water in the Pacific identified by a simulated passive tracer and its adjoint*. J. Phys. Oceanogr. https://doi.org/10.1175/2009JPO4045.1.
Radenac, M.H., Messié, M., Léger, F., Bosc, C., 2013. A very oligotrophic zone observed from space in the equatorial Pacific warm pool. Remote Sens. Environ. https://doi.org/10.1016/j.rse.2013.03.007.
Reid, J.L., 1986. On the Total Geostrophic Circulation of the South Pacific Ocean: Flow Patterns, Tracers and Transports.
Reid, J.L., 1997. On the Total Geostrophic Circulation of the Pacific Ocean: Flow Patterns, Tracers, and Transports.
Roemmich, D., Hautala, S., Rudnick, D., 1996. Northward abyssal transport through the Samoan passage and adjacent regions. Journal of Geophysical Research C: Oceans. https://doi.org/10.1029/96JC00797.
Rousseau, T.C.C., Sonke, J.E., et al., 2013. Rare earth element analysis in natural waters by multiple isotope dilution-sector field ICP-MS. J. Anal. At. Spectrom. https://doi.org/10.1039/c3ja30332b.
Rousseau, T.C.C., Sonke, J.E., et al., 2015. Rapid neodymium release to marine waters from lithogenic sediments in the Amazon estuary. Nat. Commun. https://doi.org/10.1038/ncomms8592.
Schijf, J., Christenson, E.A., Byrne, R.H., 2015. YREE scavenging in seawater: a new look at an old model. Mar. Chem. https://doi.org/10.1016/j.marchem.2015.06.010.
Shiller, A.M., Chan, E.W., Joung, D.J., Redmond, M.C., Kessler, J.D., 2017. Light rare earth element depletion during Deepwater Horizon blowout methanotrophy. Sci. Rep. 7, 10389. https://doi.org/10.1038/s41598-017-11060-z.
Sholkovitz, E., Szymczak, R., 2000. The estuarine chemistry of rare earth elements: Comparison of the Amazon, Fly, Sepik and the Gulf of Papua systems. Earth Planet. Sci. Lett. https://doi.org/10.1016/S0012-821X(00)00112-6.
Sholkovitz, E.R., Landing, W.M., Lewis, B.L., 1994. Ocean Particle Chemistry: The Fractionation of Rare Earth Elements between Suspended Particles and Seawater.
Slemons, L.O., Murray, J.W., Resing, J., Paul, B., Dutrieux, P., 2010. Western Pacific coastal sources of iron, manganese, and aluminum to the equatorial undercurrent. Glob. Biogeochem. Cycles. https://doi.org/10.1029/2009GB003693.
Sokolov, S., Rintoul, S., 2000. Circulation and water masses of the southwest Pacific: WOCE Section P11, Papua New Guinea to Tasmania. J. Mar. Res. https://doi.org/10.1357/002224000321511151.
Tachikawa, K., Athias, V., Jeandel, C., 2003. Neodymium budget in the modern ocean and paleo-oceanographicimplications. J. Geophys. Res. 108 (C8), 3254. https://doi.org/10.1029/1999JC000285.
Tachikawa, K., Jeandel, C., Roy-Barman, M., 1999. A new approach to the Nd residence time in the ocean: the role of atmospheric inputs. Earth Planet. Sci. Lett. 170, 433–446. https://doi.org/10.1016/S0012-821X(99)00127-2.
Takebe, M., 2005. This content downloaded from 142.12.73.66 on Sun. Source: The Journal of Geology 113, 201–215. https://doi.org/10.1086/427669.
Talley, L., 2007. Hydrographic Atlas of the World Ocean Circulation Experiment (WOCE). Pacific Ocean, vol. Volume 2.
Tomczak, M., Godfrey, J.S., 2003. Hydrology of the Pacific Ocean, Regional Oceanography: An Introduction, 2nd Improved Edition. Daya Publishing House, Delhi, pp. 137–174.
Tomczak, M., Hao, D., 1989. Water masses in the thermocline of the coral sea. Deep Sea Research Part A. Oceanographic Research Papers 36, 1503–1514. https://doi.org/10.1016/0198-0149(89)90054-X.
Tomczak, M., Large, D.G.B., 1989. Optimum multiparameter analysis of mixing in the thermocline of the eastern Indian Ocean. J. Geophys. Res. 94, 16141. https://doi.org/10.1029/JC094iC11p16141.
Tsimplis, M.N., Bacon, S., Bryden, H.L., 1998. The circulation of the subtropical South Pacific derived from hydrographic data. Journal of Geophysical Research: Oceans. https://doi.org/10.1029/98JC01881.
Tsuchiya, M., 1981. The origin of the Pacific equatorial 13°C water. J. Phys. Oceanogr. 11, 794–812. https://doi.org/10.1175/1520-0485(1981)011<0794:TOOTPE>2.0.CO;2.
Tsuchiya, M., Lukas, R., Fine, R.A., Firing, E., Lindstrom, E., 1989. Source waters of the Pacific Equatorial Undercurrent. Prog. Oceanogr. 23, 101–147. https://doi.org/10.1016/0079-6611(89)90012-8.
Wang, Z.L., Yamada, M., 2007. Geochemistry of dissolved rare earth elements in the equatorial Pacific ocean. Environ. Geol. https://doi.org/10.1007/s00254-006-0515-7.
Wijffels, S.E., Toole, J.M., Davis, R., 2001. Revisiting the South Pacific subtropical circulation: a synthesis of World Ocean Circulation Experiment observations along 32°S. Journal of Geophysical Research: Oceans. https://doi.org/10.1029/1999JC000118.
Zhang, J., Nozaki, Y., 1996. Rare earth elements and yttrium in seawater: ICP-MS determinations in the East Caroline, Coral Sea, and South Fiji basins of the western South Pacific Ocean. Geochim. Cosmochim. Acta. https://doi.org/10.1016/S0016-7037(96)00276-1.
Zhang, Y., Lacan, F., Jeandel, C., 2008. Dissolved rare earth elements tracing lithogenic inputs over the Kerguelen Plateau (Southern Ocean). Deep-Sea Research Part II: Topical Studies in Oceanography. https://doi.org/10.1016/j.dsr2.2007.12.029.

View publication stats

ResearchGate

See discussions, stats, and author profiles for this publication at: https://www.researchgate.net/publication/333422557

Dissolved rare earth elements distribution in the Solomon Sea

Article *in* Chemical Geology · May 2019

DOI: 10.1016/j.chemgeo.2019.05.012

CITATIONS
0

READS
65

9 authors, including:

Viet Quoc Pham
Paul Sabatier University - Toulouse III
1 PUBLICATION **0** CITATIONS

SEE PROFILE

Melanie Grenier
University of British Columbia - Vancouver
12 PUBLICATIONS **191** CITATIONS

SEE PROFILE

Sophie Cravatte
Institute of Research for Development
74 PUBLICATIONS **2,151** CITATIONS

SEE PROFILE

Some of the authors of this publication are also working on these related projects:

Project ZEBRE: study of the subthermocline currents in the Tropical Oceans View project

Project KEOPS2 View project

All content following this page was uploaded by Melanie Grenier on 18 June 2019.

The user has requested enhancement of the downloaded file.